A wave-based optimization framework for 1D and 2D periodic structures

R.F. Boukadia, E. Deckers, C. Claeys, M. Ichchou, W. Desmet

A Wave-Based Optimization Framework for 1D and 2D Periodic Structures

R. F. Boukadia[a,c,d], E. Deckers[b,c], C. Claeys[a,c], M. Ichchou[d], W. Desmet[a,c]

[a] *KU Leuven, Department of Mechanical Engineering, Division LMSD, Celestijnenlaan 300 - box 2420, Heverlee, Belgium*
[b] *KU Leuven, Diepenbeek Campus, Mechanical Engineering Technology TC, Wetenschapspark 27, 3590 Diepenbeek, Belgium*
[c] *DMMS lab, Flanders Make*
[d] *Ecole Centrale de Lyon, 36 Avenue Guy de Collongue, 69134 Ecully Cedex, France*

Abstract

This paper presents a second order optimization method based on the WFEM framework that enables the optimization of finite 1D periodic structures and 2D infinite ones. While optimization at the unit cell level has been done in previous studies, it did not account for the boundary conditions and excitation on the system, which might have an important influence on its dynamics. The proposed methodology exploits semi-analytical derivatives in an optimization algorithm that combines line search and trust region methods. It is tested and validated in a parameter identification procedure and subsequently used to minimize the mean square velocity of metabeams with clamped free boundary conditions. Finally, it is applied to the optimization of the sound transmission loss of a metapanel in the structural-acoustic coincidence region. The proposed scheme is versatile and can be used in a wide range of applications including, model updating, homogenization, design optimization and possibly damage detection.

Keywords: Optimization, WFEM, Boundary Conditions, Metamaterials, Periodic Structures

Email address: regis.boukadia@kuleuven.be (R. F. Boukadia)

1. Introduction

As constraints on the weight and volume of vibro-acoustic packages become more important, the interest in metamaterial based solutions increases. This interest is mostly driven by the stopband behavior exhibited by some periodic structures enabling sound insulation properties that go beyond the mass law. So far, the Wave Finite Element Method [1, 2, 3] and the Shift Cell Operator Method [4] have been the most popular tools to study and engineer smart structures based on this concept because they allow the computation of the dispersion characteristics of a periodic medium by the discretization of a single unit cell (UC). Studies based on the analysis of dispersion curves and band diagrams have become standard and designs including perforations or resonant add-ons have been used to open bandgaps around targeted frequencies [5, 6, 7, 8, 9]. More recently, numerical methods have been developed to obtain bandgaps with maximal width and attenuation properties in phononic crystals [10, 11] or specific anisotropic behavior in meta-structures [12]. However, most of the studies in the literature focus purely on the prediction of stopbands without investigating the impact of boundary conditions, operating environment, load characteristics and finite size effects on the performance of metamaterial solutions. While those topics have been studied from a theoretical or qualitative point of view [13, 14, 15, 16], not many studies deal with them applying detailed numerical modeling [17]. This paper presents a second order optimization framework based on the WFEM that overcomes most of these issues. The proposed framework combines semianalytical derivatives computed via an intrusive procedure to a second order optimization algorithm. Because this class of algorithms has been successfully applied to structural optimization and parameter identification problems [18, 19, 20, 21], the proposed optimization algorithm was designed to be an instance of Sequential Quadratic Programming (SQP). It incorporates both an ellipsoidal trust-region method and a line search method [22]. The former method ensures that the optimization algorithm rapidly escapes saddle points in regions of negative curvature [23, 24] while the latter usually performs better in neighbourhoods where the optimized function is convex. For 1D periodic structures, loads, boundary conditions and structure size can all be accounted for by the proposed framework. This is because formulations for the forced response of periodic waveguides and coupled periodic waveguides have been developed [3, 25]. In the 2D case, only the loads' spatial characteristics (TBL, plane waves, punctual source) can be included because a formulation for the forced response of finite 2D periodic structures has yet to be developed.

The rest of the paper is organized as follows. Section 2 briefly recaps the theory behind the direct 1D WFEM and presents formulas for derivatives in that framework. Section 3 presents the indirect 2D WFEM and the associated infinite forced response scheme. Formulas for the derivatives of eigenfrequencies, waveshapes and displacements are also provided. In Section 4, a second order optimization algorithm is presented and used for the numerical examples of Section 5. Section 6 summarizes the main conclusions.

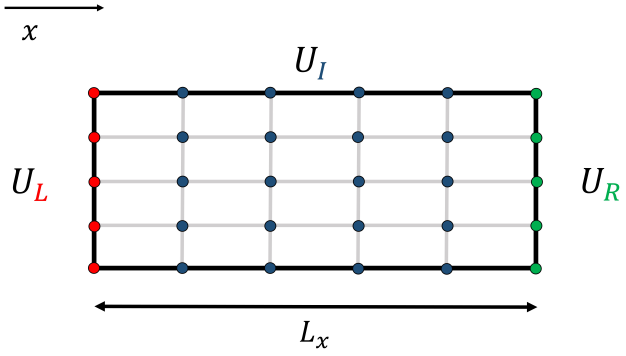

Figure 1: Dofs' partition for the UC of a 1D periodic structure

2. 1D WFEM

In this section, derivatives for propagation constants, waveshapes and forced response computed using the 1D WFEM are derived. Using the proposed analytical formulas, it is possible to compute the gradient and hessian matrix of objective functions considered in Section 5 at relatively low computational cost. These can then be used in the algorithm described in Section 4 to optimize periodic structures in a unit cell modeling framework. Section 2 is organized as follows. First, subsection 2.1 recaps the theory and main steps of the direct 1D WFEM while subsection 2.2 focuses on the derivatives' computation.

2.1. Wavenumber, Waveshpapes, Forced Response

The mass matrix M, stiffness matrix K and damping matrix C of a periodic structure's UC are considered. A partition of its degrees of freedom U is established according to the UC's spatial structure (see Figure 1):

$$U = \begin{bmatrix} U_L \\ U_I \\ U_R \end{bmatrix} \tag{1}$$

The subscripts R, L and I are used for variables associated with the right, left and internal dofs of the UC, respectively. Additionally, the subscript B will be used for quantities associated to all interface dofs. The first step in the direct formulation of the 1D WFEM is to compute the dynamic stiffness matrix G for a given circular frequency ω:

$$G = K + i\omega C - \omega^2 M \tag{2}$$

The internal dofs of the UC are then condensed out in order to form the condensed dynamic stiffness matrix D:

$$D = G_{BB} - G_{BI} G_{II}^{-1} G_{IB} \tag{3}$$

Applying Floquet-Bloch boundary conditions $U_R = \lambda U_L$ (displacement), $F_R = -\lambda F_L$ (load) leads to the eigenvalue problem [26]:

$$\left(\lambda D_{LR} + (D_{LL} + D_{RR}) + \frac{1}{\lambda} D_{RL}\right)\Psi = 0 \tag{4}$$

The propagation constant λ is related to the wavenumber k_x via the relation $\lambda = e^{-ik_x L_x}$, L_x being the length of the UC in the direction of propagation. The eigenvalue problem (4) yields the waveshapes Ψ_k and propagation constants λ_k of free waves in the periodic medium at the circular frequency ω. It should be noted that the propagation constants come in pairs $\left(\lambda_k, \frac{1}{\lambda_k}\right)$ with eigenvectors $\left(\Psi_k^+, \Psi_k^-\right)$ that correspond to waves traveling in the positive and negative direction. For passive structures, direction of propagation and direction of decay coincide, therefore, positives going waves correspond to $|\lambda| \leq 1$ and negative going waves to $|\lambda| \geq 1$. In case $\lambda \approx 1$, positive going wave have a positive powerflow and negative going waves a negative one [27]. For active structures, waves should be sorted according to their direction of decay to solve equation (5) hence the proposed sorting method may still be used. Once propagation constants and waveshapes are properly sorted, it is possible to compute the forced response of a finite waveguide comprised of N UCs by relating the waves' amplitudes to the excitations and boundary conditions. The specific case of Clamped-Free boundary conditions is detailed in equation (5) as it is used in Section 5 but similar formulas are available for other types of boundary conditions [25, 3, 28]:

$$\begin{pmatrix} \Psi^+ & \Psi^-\Lambda^N \\ D_{RL}\Psi^+\Lambda^{N-1} + D_{RR}\Psi^+\Lambda^N & D_{RL}\Psi^-\Lambda + D_{RR}\Psi^- \end{pmatrix} \begin{bmatrix} q^+ \\ q^- \end{bmatrix} = \begin{bmatrix} V_0 \\ F_N \end{bmatrix} \tag{5}$$

In equation (5), q^+ and q^- are the vectors of the positive and negative going waves' amplitudes. V_0 is the imposed displacement at the left side of the waweguide while F_N is the force applied at its right side. Ψ^+ is an n by n matrix whose columns are the eigenvectors Ψ_k^+ corresponding to positive going waves. Likewise, Ψ^- is formed with the eigenvectors Ψ_k^- of the negative going waves. Λ is a diagonal matrix with the positive propagation constants λ_k on the diagonal. The displacement of the i^{th} section of the waveguide is given by equation (6):

$$V_i = \Psi^+\Lambda^i q^+ + \Psi^-\Lambda^{N-i} q^- \tag{6}$$

2.2. Derivatives in the 1D WFEM Framework

In order to optimize a UC to obtain a desired behavior, some properties of the UC are parametrized. The vector of these m parameters is noted $p = (p_1, ..., p_m) \in \mathbb{R}^m$. It follows that the mass, stiffness and damping matrix, $M(p)$, $K(p)$, $C(p)$ are functions of the parameter vector p. Assuming the first and second order derivatives of the matrices with respect to p are available, the derivatives of all the quantities derived in Subsection 2.1 can be computed. For a given circular frequency ω the first order derivatives of the dynamic stiffness matrix are:

$$\frac{\partial G}{\partial p_k} = \frac{\partial K}{\partial p_k} + i\omega\frac{\partial C}{\partial p_k} - \omega^2\frac{\partial M}{\partial p_k} \tag{7}$$

Likewise, the second order derivatives of the dynamic stiffness matrix are:

$$\frac{\partial^2 G}{\partial p_k \partial p_l} = \frac{\partial^2 K}{\partial p_k \partial p_l} + i\omega\frac{\partial^2 C}{\partial p_k \partial p_l} - \omega^2\frac{\partial^2 M}{\partial p_k \partial p_l} \tag{8}$$

Using equation (3), the derivatives of the condensed dynamic stiffness matrix can be derived:

$$\frac{\partial D}{\partial p_k} = \frac{\partial G_{BB}}{\partial p_k} - \left(\frac{\partial G_{BI}}{\partial p_k} G_{II}^{-1} G_{IB} - G_{BI} G_{II}^{-1} \frac{\partial G_{II}}{\partial p_k} G_{II}^{-1} G_{IB} + G_{BI} G_{II}^{-1} \frac{\partial G_{IB}}{\partial p_k} \right) \tag{9}$$

Taking advantage of the fact that G and D are symmetric matrices this can be rewritten as:

$$\frac{\partial D}{\partial p_k} = \frac{\partial G_{BB}}{\partial p_k} + \Theta_{IB}^T \frac{\partial G_{II}}{\partial p_k} \Theta_{IB} - 2sym\left(\Theta_{IB}^T \frac{\partial G_{IB}}{\partial p_k} \right) \tag{10}$$

With:

$$\begin{cases} \Theta_{IB} = G_{II}^{-1} G_{IB} \\ sym(A) = \dfrac{1}{2}\left(A + A^T\right) \end{cases} \tag{11}$$

That way, Θ_{IB} needs only to be computed once and all first order derivatives of D can be computed without additional matrix inversions. Following that trend, the second order derivatives of D are obtained:

$$\frac{\partial^2 D}{\partial p_k \partial p_l} = \frac{\partial^2 G_{BB}}{\partial p_k \partial p_l} + \Theta_{IB}^T \frac{\partial^2 G_{II}}{\partial p_k \partial p_l} \Theta_{IB} + 2sym\left[\frac{\partial \Theta_{IB}^T}{\partial p_l} \left(\frac{\partial G_{II}}{\partial p_k} \Theta_{IB} - \frac{\partial G_{IB}}{\partial p_k} \right) - \Theta_{IB}^T \frac{\partial^2 G_{IB}}{\partial p_k \partial p_l} \right] \tag{12}$$

With:

$$\frac{\partial \Theta_{IB}}{\partial p_l} = G_{II}^{-1} \left(-\frac{\partial^2 G_{II}}{\partial p_l} \Theta_{IB} + \frac{\partial G_{IB}}{\partial p_l} \right) \tag{13}$$

Equation (12) and (13) show that it is necessary to invert G_{II} m times to compute all derivatives of D. Consequently, keeping the LU decomposition of G_{II} the first time this operation is performed allows to reduce the computation time of the derivatives' evaluation. The derivatives of propagation constants and waveshapes can be computed by using formulas of Appendix B with:

$$X(\lambda, p) = \lambda D_{LR}(p) + (D_{LL}(p) + D_{RR}(p)) + \frac{1}{\lambda} D_{RL}(p) \tag{14}$$

In order to keep formulas shorter we introduce the following matrix functions:

$$\begin{cases} \dfrac{\partial X(\lambda,p)}{\partial p_k} = \lambda \dfrac{\partial D_{LR}}{\partial p_k} + \left(\dfrac{\partial D_{RR}}{\partial p_k} + \dfrac{\partial D_{LL}}{\partial p_k} \right) + \dfrac{1}{\lambda} \dfrac{\partial D_{RL}}{\partial p_k} \\ \dfrac{\partial X(\lambda,p)}{\partial \lambda} = D_{LR} - \dfrac{1}{\lambda^2} D_{RL} \\ \dfrac{dX(\lambda,p)}{dp_k} = \dfrac{\partial X(\lambda,p)}{\partial p_k} + \dfrac{\partial \lambda}{\partial p_k} \dfrac{\partial X(\lambda,p)}{\partial \lambda} \\ \dfrac{\partial^2 X(\lambda,p)}{\partial \lambda^2} = \dfrac{2}{\lambda^3} D_{RL} \\ \dfrac{\partial^2 X(\lambda,p)}{\partial \lambda \partial p_k} = \dfrac{\partial D_{LR}}{\partial p_k} - \dfrac{1}{\lambda^2} \dfrac{\partial D_{RL}}{\partial p_k} \\ \dfrac{\partial^2 X(\lambda,p)}{\partial p_k \partial p_l} = \lambda \dfrac{\partial D_{LR}}{\partial p_k \partial p_l} + \left(\dfrac{\partial D_{RR}}{\partial p_k \partial p_l} + \dfrac{\partial D_{LL}}{\partial p_k \partial p_l} \right) + \dfrac{1}{\lambda} \dfrac{\partial^2 D_{RL}}{\partial p_k \partial p_l} \\ \dfrac{d^2 X(\lambda,p)}{dp_k dp_l} = \dfrac{\partial^2 X(\lambda,p)}{\partial p_k \partial p_l} + \dfrac{\partial \lambda}{\partial p_l} \dfrac{\partial^2 X(\lambda,p)}{\partial \lambda \partial p_k} + \dfrac{\partial \lambda}{\partial p_k} \dfrac{\partial^2 X(\lambda,p)}{\partial \lambda \partial p_l} + \dfrac{\partial^2 \lambda}{\partial p_k \partial p_l} \dfrac{\partial X(\lambda,p)}{\partial \lambda} + \dfrac{\partial \lambda}{\partial p_k} \dfrac{\partial \lambda}{\partial p_l} \dfrac{\partial^2 X(\lambda,p)}{\partial \lambda^2} \end{cases} \tag{15}$$

It should also be considered that the parametric eigenvalue problem (14) is T-palindromic [29]. This means the eigenvalues comes in pairs $\left(\lambda_i, \frac{1}{\lambda_i}\right)$ and that the right eigenvector for λ_i, Ψ_i, is the left eigenvector for $\frac{1}{\lambda_i}$. Conversely,

the right eigenvector for $\frac{1}{\lambda_i}$, Φ_i, is the left eigenvector for λ_i. Because of this feature computing the left eigenvectors of (14) is not required to evaluate the derivatives. Applying formulas from Appendix B the first order derivatives for the propagation constants and the waveshapes are derived:

$$\frac{\partial \lambda_i}{\partial p_k}\Phi_i^T\left(D_{LR}-\frac{1}{\lambda_i^2}D_{RL}\right)\Psi_i=-\Phi_i^T\left[\lambda_i\frac{\partial D_{LR}}{\partial p_k}+\left(\frac{\partial D_{RR}}{\partial p_k}+\frac{\partial D_{LL}}{\partial p_k}\right)+\frac{1}{\lambda_i}\frac{\partial D_{RL}}{\partial p_k}\right]\Psi_i \tag{16}$$

$$\frac{\partial \Psi_i}{\partial p_k}=-X^+(\lambda_i,p)\left[\left(\frac{\partial \lambda_i}{\partial p_k}D_{LR}+\lambda_i\frac{\partial D_{LR}}{\partial p_k}\right)+\left(\frac{\partial D_{RR}}{\partial p_k}+\frac{\partial D_{LL}}{\partial p_k}\right)+\left(-\frac{\partial \lambda_i}{\partial p_k}\frac{1}{\lambda_i^2}D_{RL}+\frac{1}{\lambda_i}\frac{\partial D_{RL}}{\partial p_k}\right)\right]\Psi_i \tag{17}$$

For the second order derivatives, equations (B.11) and (B.12) are used with the expressions given in equation (15):

$$\frac{d^2\lambda_i}{\partial p_k\partial p_l}\left(\Phi_i^T\frac{\partial X}{\partial \lambda}\Psi_i\right)=-\Phi_i^T\left[\left(\frac{\partial^2 X}{\partial p_l\partial p_k}+\frac{\partial \lambda}{\partial p_l}\frac{\partial^2 X}{\partial \lambda\partial p_k}+\frac{\partial \lambda}{\partial p_k}\frac{\partial^2 X}{\partial \lambda\partial p_l}+\frac{\partial \lambda}{\partial p_k}\frac{\partial \lambda}{\partial p_l}\frac{\partial^2 X}{\partial \lambda^2}\right)\Psi_i+\left(\frac{dX}{dp_k}\frac{\partial \Psi_i}{\partial p_l}+\frac{dX}{dp_l}\frac{\partial \Psi_i}{\partial p_k}\right)\right] \tag{18}$$

$$\frac{\partial^2\Psi_i}{\partial p_l\partial p_k}=-X^+\left(\frac{d^2X}{dp_kdp_l}\Psi_i+\frac{dX}{dp_k}\frac{\partial \Psi i}{\partial p_l}+\frac{dX}{dp_l}\frac{\partial \Psi_i}{\partial p_k}\right)-\Re\left(\left(\frac{\partial \Psi_i}{\partial p_l}\middle|\frac{\partial \Psi_i}{\partial p_k}\right)\right)\Psi_i \tag{19}$$

The derivatives of the wave coefficients should be computed according to Appendix A. First, equation (5) is rewritten to simplify the expression of the derivatives:

$$WQ=\begin{pmatrix}W_{11} & W_{12}\\ W_{21} & W_{22}\end{pmatrix}\begin{bmatrix}q^+\\ q^-\end{bmatrix}=\begin{bmatrix}V_0\\ F_N\end{bmatrix} \tag{20}$$

Then using equations (A.4) and (A.5) expressions for the first and second order derivatives of the wave coefficients are given:

$$\frac{\partial Q}{\partial p_i}=-W^{-1}\frac{\partial W}{\partial p_i}Q \tag{21}$$

$$\frac{\partial^2 Q}{\partial p_i\partial p_j}=-W^{-1}\left(\frac{\partial^2 W}{\partial p_i\partial p_j}Q+\frac{\partial W}{\partial p_i}\frac{\partial Q}{\partial p_j}+\frac{\partial W}{\partial p_j}\frac{\partial Q}{\partial p_i}\right) \tag{22}$$

Expressions for the derivatives of W are given in Appendix C. Once the derivatives of the wave coefficients are computed, the derivatives of the displacement at the i^{th} section of the waveguide follow:

$$\frac{\partial V_i}{\partial p_k}=\frac{\partial \Psi^+}{\partial p_k}\Lambda^i q^+ + i\Psi^+\frac{\partial \Lambda}{\partial p_k}\Lambda^{i-1}q^+ + \Psi^+\Lambda^i\frac{\partial q^+}{\partial p_k}+\frac{\partial \Psi^-}{\partial p_k}\Lambda^{N-i}q^- + (N-i)\Psi^-\frac{\partial \Lambda}{\partial p_k}\Lambda^{N-i-1}q^- + \Psi^-\Lambda^{N-i}\frac{\partial q^-}{\partial p_k} \tag{23}$$

$$\begin{aligned}\frac{\partial^2 V_i}{\partial p_k\partial p_l}=&\frac{\partial^2\Psi^+}{\partial p_k}\Lambda^i q^+ + \Psi^+\Lambda^i\frac{\partial^2 q^+}{\partial p_k\partial p_l}+\frac{\partial \Psi^+}{\partial p_k}\Lambda^i\frac{\partial q^+}{\partial p_l}+\frac{\partial \Psi^+}{\partial p_l}\Lambda^i\frac{\partial q^+}{\partial p_k}\\ &+i\left(\frac{\partial \Psi^+}{\partial p_k}\frac{\partial \Lambda}{\partial p_l}\Lambda^{i-1}q^+ + \frac{\partial \Psi^+}{\partial p_l}\frac{\partial \Lambda}{\partial p_k}\Lambda^{i-1}q^+ + \Psi^+\frac{\partial \Lambda}{\partial p_k}\Lambda^{i-1}\frac{\partial q^+}{\partial p_l}+\Psi^+\frac{\partial \Lambda}{\partial p_l}\Lambda^{i-1}\frac{\partial q^+}{\partial p_k}\right)\\ &+i(i-1)\Psi^+\frac{\partial \Lambda}{\partial p_k}\frac{\partial \Lambda}{\partial p_l}\Lambda^{i-2}q^+\\ &+\frac{\partial^2\Psi^-}{\partial p_k}\Lambda^{N-i}q^- + \Psi^-\Lambda^{N-i}\frac{\partial^2 q^-}{\partial p_k\partial p_l}+\frac{\partial \Psi^-}{\partial p_k}\Lambda^{N-i}\frac{\partial q^-}{\partial p_l}+\frac{\partial \Psi^-}{\partial p_l}\Lambda^{N-i}\frac{\partial q^-}{\partial p_k}+\\ &+(N-i)\left(\frac{\partial \Psi^-}{\partial p_k}\frac{\partial \Lambda}{\partial p_l}\Lambda^{N-i-1}q^- + \frac{\partial \Psi^-}{\partial p_l}\frac{\partial \Lambda}{\partial p_k}\Lambda^{N-i-1}q^- + \Psi^-\frac{\partial \Lambda}{\partial p_k}\Lambda^{N-i-1}\frac{\partial q^-}{\partial p_l}+\Psi^-\frac{\partial \Lambda}{\partial p_l}\Lambda^{N-i-1}\frac{\partial q^-}{\partial p_k}\right)\\ &+(N-i-1)(N-i-2)Psi^-\frac{\partial \Lambda}{\partial p_k}\frac{\partial \Lambda}{\partial p_l}\Lambda^{N-i-2}q^-\end{aligned} \tag{24}$$

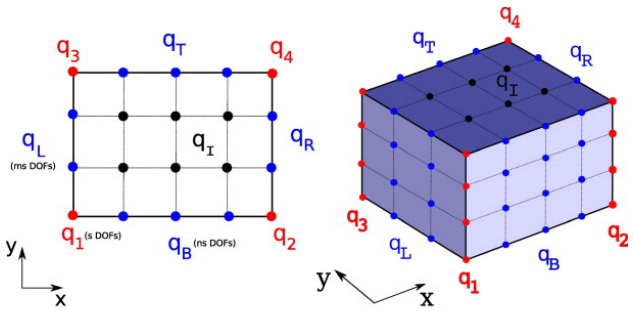

(a) View from the top (b) View 3D

Figure 2: Dofs' partition of a 2D UC

3. 2D WFEM

In this section, derivatives for eigenfrequencies, waveshapes and displacements computed using the inverse 2D WFEM are derived. Using the proposed analytical formulas, it is possible to compute the gradient and hessian matrix of objective functions considered in Section 5 at relatively low computational cost. They can then be used in the algorithm described in Section 4 to optimize periodic structures in a unit cell modeling framework. Section 3 is organized as follows. First, subsection 3.1 recaps the theory and main steps of the indirect 2D WFEM while subsection 3.2 focuses on the derivatives' computation.

3.1. Band diagram and response to loads with Floquet-Bloch Symmetry

Similarly to the 1D case, the 2D WFEM applies Floquet-Bloch boundary conditions a posteriori on the discretized model of the UC. The stiffness, mass and damping matrix of the UC are noted K, M and C respectively. The UC's displacement vector is referred to as U. The dofs of the UC are partitioned following its spatial structure as illustrated in Figure 2, taken from [30]:

$$U = \begin{bmatrix} q_1 & q_2 & q_3 & q_4 & q_L & q_R & q_B & q_T & q_I \end{bmatrix}^T \tag{25}$$

The numbers of dofs in q_1, q_2, q_3 and q_4 are identical and noted n_1. Likewise, the number of dofs in q_L and q_R is noted n_L. For q_B and q_T n_B is used while n_I is used for q_I. The inverse form of the 2D WFEM proceeds by choosing two wavenumbers (k_x, k_y) and enforcing the corresponding Floquet-Bloch boundary conditions on the UC:

$$q_2 = \lambda_x q_1,\ q_3 = \lambda_y q_1,\ q_4 = \lambda_x \lambda_y q_1,\ q_R = \lambda_x q_L,\ q_T = \lambda_y q_B \tag{26}$$

$$\begin{cases} f_1 + \dfrac{f_2}{\lambda_x} + \dfrac{f_3}{\lambda_y} + \dfrac{f_4}{\lambda_x \lambda_y} = 0 \\ f_L + \dfrac{f_R}{\lambda_x} = 0 \\ f_B + \dfrac{f_T}{\lambda_y} = 0 \end{cases} \tag{27}$$

In equations (26) and (27) λ_x and λ_y are the propagation constants in the x and y direction and are related to the wavenumbers (k_x, k_y) in the periodic medium via the side lengths of the UC, L_x and L_y respectively:

$$\lambda_x = e^{-ik_x L_x},\ \lambda_y = e^{-ik_y L_y} \tag{28}$$

The Floquet-Bloch boundary conditions are enforced using two projection matrices P_U and P_F (see [31]):

$$U = P_U(k_x, k_y)U_r = \begin{pmatrix} I_{n_1} & 0 & 0 & 0 \\ \lambda_x I_{n_1} & 0 & 0 & 0 \\ \lambda_y I_{n_1} & 0 & 0 & 0 \\ \lambda_x\lambda_y I_{n_1} & 0 & 0 & 0 \\ 0 & I_{n_L} & 0 & 0 \\ 0 & \lambda_x I_{n_L} & 0 & 0 \\ 0 & 0 & I_{n_B} & 0 \\ 0 & 0 & \lambda_y I_{n_B} & 0 \\ 0 & 0 & 0 & I_{n_C} \end{pmatrix} \begin{bmatrix} q_1 \\ q_L \\ q_B \\ q_I \end{bmatrix} \tag{29}$$

$$P_F(k_x, k_y) = \begin{pmatrix} I & \frac{1}{\lambda_x} I_{n_1} & \frac{1}{\lambda_y} I_{n_1} & \frac{1}{\lambda_x\lambda_y} I_{n_1} & 0 & 0 & 0 & 0 & 0 \\ 0 & 0 & 0 & 0 & I_{n_L} & \frac{1}{\lambda_x} I_{n_L} & 0 & 0 & 0 \\ 0 & 0 & 0 & 0 & 0 & 0 & I_{n_B} & \frac{1}{\lambda_y} I_{n_B} & 0 \\ 0 & 0 & 0 & 0 & 0 & 0 & 0 & 0 & I_{n_C} \end{pmatrix} \tag{30}$$

By enforcing these relations a modified equation of the dynamics whose validity is restrained to loads and displacements satisfying the Floquet-Bloch conditions associated to the wavenumber pair (k_x, k_y) is derived:

$$\left[K(k_x, k_y) + i\omega C(k_x, k_y) - \omega^2 M(k_x, k_y)\right] U_r = D(k_x, k_y)U_r = F_r \tag{31}$$

For a generic matrix $A \in M_n(\mathbb{C})$, the matrix $A(k_x, k_y)$ is derived from matrix A according to equation (32).

$$A(k_x, k_y) = P_F(k_k, k_y)AP_U(k_x, k_y); \tag{32}$$

Equation (31) can be used to compute the response of an infinite periodic medium to a load with 2D Floquet-Bloch symmetry (such as a plane wave) or to compute its band diagram when there is no load [32]:

$$\left[K(k_x, k_y) + i\omega_r C(k_x, k_y) - \omega_r^2 M(k_x, k_y)\right] \Psi_r = 0 \tag{33}$$

In most cases, the eigenvalue problem (33) is solved with k_x and k_y as real numbers. This means $\frac{1}{\lambda_x} = \overline{\lambda_x}$, $\frac{1}{\lambda_y} = \overline{\lambda_y}$ thus $P_F = P_U^*$ which results in all matrices in (33) being hermitian. The eigenvalues come in pairs $(\omega_r, -\overline{\omega_r})$ with eigenvectors (Ψ_r, Φ_r). Additionally, $\overline{\Psi_r}$ is the left eigenvector for $-\overline{\omega_r}$, therefore only the right eigenvectors of (33) need to be computed.

3.2. Derivatives in the 2D WFEM Framework

As in the 1D case, some properties of the UC are parametrized in order to optimize for a specific behavior. The vector of these m parameters is noted $p = (p_1, ..., p_m) \in \mathbb{R}^m$. It follows that the mass, stiffness and damping matrix, respectively $M(p)$, $K(p)$ and $C(p)$, are functions of the parameter vector p. It is also assumed that the first and second order derivatives of the matrices with respect to p are available. Under these assumptions, the derivatives of all the quantities defined in Subsection 3.1 can be computed. Starting with equation (31), the derivatives of the modified dynamic stiffness matrix are:

$$\frac{\partial D(k_x,k_y)}{\partial pk} = P_F(k_x,k_y)\left(\frac{\partial K}{\partial pk} + i\omega\frac{\partial C}{\partial pk} - \omega^2\frac{\partial M}{\partial pk}\right)P_U(k_x,k_y) \tag{34}$$

$$\frac{\partial^2 D(k_x,k_y)}{\partial pk\partial p_l} = P_F(k_x,k_y)\left(\frac{\partial^2 K}{\partial pk\partial p_l} + i\omega\frac{\partial^2 C}{\partial pk\partial p_l} - \omega^2\frac{\partial^2 M}{\partial pk\partial p_l}\right)P_U(k_x,k_y) \tag{35}$$

Using equations (A.4) and (A.5) the derivatives of U_r are derived:

$$\frac{\partial U_r}{\partial p_k} = -D^{-1}(k_x,k_y)\frac{\partial D(k_x,k_y)}{\partial p_k}U_r \tag{36}$$

$$\frac{\partial^2 U_r}{\partial p_k\partial p_l} = -D^{-1}(k_x,k_y)\left(\frac{\partial^2 D(k_x,k_y)}{\partial p_k\partial p_l}U_r + \frac{\partial D(k_x,k_y)}{\partial p_k}\frac{\partial U_r}{\partial p_l} + \frac{\partial D(k_x,k_y)}{\partial p_l}\frac{\partial U_r}{\partial p_k}\right) \tag{37}$$

To efficiently compute the derivatives of U_r, it is important that the LU decomposition of $D(k_x, k_y)$ is performed only once and reused in all matrix-vector inversions. Finally, the derivatives of the waveshapes Ψ_r and eigenfrequencies ω_r are derived using Appendix B with the parametric matrix:

$$D(k_x,k_y,\omega,p) = K(k_x,k_y,p) + i\omega C(k_x,k_y,p) - \omega^2 M(k_x,k_y,p) \tag{38}$$

In order to increase readability, the dependency in p will be omitted. Moreover, the following matrix functions are defined:

$$\begin{cases}
\dfrac{\partial D(k_x,k_y,\omega_r)}{\partial p_k} = \dfrac{\partial K(k_x,k_y)}{\partial pk} + i\omega_r\dfrac{\partial C(k_x,k_y)}{\partial pk} - \omega_r^2\dfrac{\partial M(k_x,k_y)}{\partial pk} \\
\dfrac{\partial D(k_x,k_y,\omega)}{\partial \omega} = iC(k_x,k_y) - 2\omega M(k_x,k_y) \\
\dfrac{dD(k_x,k_y,\omega)}{dp_k} = \dfrac{\partial D(k_x,k_y,\omega)}{\partial p_k} + \dfrac{\partial \omega}{\partial p_k}\dfrac{\partial D(k_x,k_y,\omega)}{\partial \omega} \\
\dfrac{\partial^2 D(k_x,k_y,\omega)}{\partial \omega^2} = -2M(k_x,k_y) \\
\dfrac{\partial^2 D(k_x,k_y,\omega)}{\partial \omega\partial p_k} = i\dfrac{\partial C(k_x,k_y)}{\partial p_k} - 2\omega\dfrac{M(k_x,k_y)}{\partial p_k} \\
\dfrac{\partial^2 D(k_x,k_y,\omega)}{\partial p_k\partial p_l} = \dfrac{\partial^2 K(k_x,k_y)}{\partial pk\partial p_l} + i\omega\dfrac{\partial^2 C(k_x,k_y)}{\partial pk\partial p_l} - \omega^2\dfrac{\partial^2 M(k_x,k_y)}{\partial pk\partial p_l} \\
\dfrac{d^2 D(k_x,k_y,\omega)}{dp_k dp_l} = \dfrac{\partial^2 D(k_x,k_y,\omega)}{\partial p_k\partial p_l} + \dfrac{\partial \omega}{\partial p_l}\dfrac{\partial D(k_x,k_y,\omega)}{\partial \omega\partial p_k} + \dfrac{\partial \omega}{\partial p_k}\dfrac{\partial D(k_x,k_y,\omega)}{\partial \omega\partial p_l} + \dfrac{\partial^2 \omega}{\partial p_k\partial p_l}\dfrac{\partial D(k_x,k_y,\omega)}{\partial \omega} \\
\qquad\qquad + \dfrac{\partial \omega}{\partial p_k}\dfrac{\partial \omega}{\partial p_l}\dfrac{\partial^2 D(k_x,k_y,\omega)}{\partial \omega^2}
\end{cases} \tag{39}$$

The first order derivatives of the eigenvalues and eigenvectors are given in equations (40) and (41) according to the formulas of Appendix B:

$$\frac{\partial \omega_r}{\partial p_k}\left(\Phi_r^T \frac{\partial D(k_x,k_y,\omega_r)}{\partial \omega}\Psi_r\right) = \left(\Phi_r^T \frac{\partial D(k_x,k_y,\omega_r)}{\partial p_k}\Psi_r\right) \tag{40}$$

$$\frac{\partial \Psi_r}{\partial p_k} = -D^+(k_x,k_y,\omega_r)\left(\frac{dD(k_x,k_y,\omega_r)}{dp_k}\Psi_r\right) \tag{41}$$

Likewise, their second order derivatives are:

$$\begin{aligned}\frac{\partial^2 \omega_r}{\partial p_k \partial p_l}\left(\Phi_r^T \frac{\partial D(k_x,k_y,\omega_r)}{\partial \omega}\Psi_r\right) =& \Phi_r^T\left(\frac{\partial^2 D(k_x,k_y,\omega)}{\partial p_k \partial p_l} + \frac{\partial \omega}{\partial p_l}\frac{\partial D(k_x,k_y,\omega)}{\partial \omega \partial p_k} + \frac{\partial \omega}{\partial p_k}\frac{\partial D(k_x,k_y,\omega)}{\partial \omega \partial p_l}\right)\Psi_r + \\ & \Phi_r^T\left(\frac{\partial \omega}{\partial p_k}\frac{\partial \omega}{\partial p_l}\frac{\partial^2 D(k_x,k_y,\omega)}{\partial \omega^2}\right)\Psi_r + \\ & \Phi_r^T\left(\frac{dD(k_x,k_y,\omega)}{dp_k}\frac{\partial \Psi_r}{\partial p_l} + \frac{dD(k_x,k_y,\omega)}{dp_l}\frac{\partial \Psi_r}{\partial p_k}\right)\end{aligned} \tag{42}$$

$$\frac{\partial^2 \Psi_r}{\partial p_k \partial p_l} = -D^+(k_x,k_y,\omega_r)\left(\frac{d^2 D(k_x,k_y,\omega)}{dp_k dp_l}\Psi_r + \frac{dD(k_x,k_y,\omega)}{dp_k}\frac{\partial \Psi_r}{\partial p_l} + \frac{dD(k_x,k_y,\omega)}{dp_l}\frac{\partial \Psi_r}{\partial p_k}\right) - \Re\left(\left(\frac{\partial \Psi_r}{\partial p_l}\middle|\frac{\partial \Psi_r}{\partial p_k}\right)\right)\Psi_r \tag{43}$$

4. Second Order Optimization Algorithm

This Section describes the second order optimization strategy used in the examples of Section 5. The strategy is developed to account for two characteristics of the Direct 1D WFEM. Firstly, obtaining accurate derivatives by numerical differentiation is difficult due to the low numerical accuracy of the WFEM as compared to usual FEM modeling [26]. Secondly, computing the response of a waveguide is relatively cheap because all computations are done based on a single UC. It follows that semi-analytical gradients and Hessians of C^2 objective functions can be computed at an acceptable cost. Making use of the available second order information, an algorithm that combines both line search and trust region methods is designed. The ellipsoidal trust-region approach [23, 24] is based on a transformation of the local Hessian matrix of the objective function and ensures that the algorithm quickly escapes saddle points in regions of negative curvature while the line search method performs better in neighborhoods where the optimized function is convex. Because of these exotic features the proposed algorithm was implemented in Matlab. It is an instance of sequential quadratic programming (SQP) [22, Chapter 18] thus possesses all the convergence properties of that class of algorithms. An objective function f and the vector of optimization variables $p \in \mathbb{R}^m$ are introduced. The variables may be subject to n_e linear equality constraints:

$$\forall i \in [\![1, n_e]\!],\ E_i(p) = 0 \tag{44}$$

And n_c convex inequality constraints:

$$\forall j \in [\![1, n_c]\!],\ C_j(p) \leq 0 \tag{45}$$

For a starting point p_0, the function's value $f(p_0)$, the gradient $\nabla f(p_0)$ and the Hessian $\nabla^2 f(p_0)$ are computed. A surrogate function $\tilde{f}$ approximating f around p_0 is introduced:

$$f(p) \approx \tilde{f}(p) = f(p_0) + \nabla f(p_0)(p - p_0) + \frac{1}{2}(p - p_0)^T \nabla^2 f(p_0)(p - p_0) \tag{46}$$

If the Hessian is positive definite, a line search method is used [22, Chapter 3]. First, the search direction ν is computed:

$$\nu = argmin\left\{\tilde{f}(p_0 + \nu),\ E_i(p) = 0,\ C_j(p) \leq 0\right\} \tag{47}$$

Equation (47) can be solved using the interior point method [22, Chapter 19] or analytically when there are no constraints. Once the search ν is computed, f is minimized in the corresponding direction:

$$\alpha_m = argmin\left\{f(p_0 + \alpha\nu), \alpha \in [0, 1]\right\} \tag{48}$$

Defining the next iteration:

$$p_1 = p_0 + \alpha_m\nu \tag{49}$$

When the Hessian is not positive definite, a trust region method [22, 23, 24, 33] is used. First, the matrix $\left|\nabla^2 f(p_0)\right|$ is defined. This matrix is obtained by keeping the eigenvectors of $\nabla^2 f(p_0)$ and taking the absolute value of all its eigenvalues. A supplementary constraint is then introduced:

$$T(p) = (p - p_0)^T \left|\nabla^2 f(p_0)\right| (p - p_0) - R_0^2 \leq 0 \tag{50}$$

The next iteration is defined as:

$$p_1 = argmin\left\{\tilde{f}(p),\ T(p) \leq 0,\ E_i(p) = 0,\ C_j(p) \leq 0\right\} \tag{51}$$

The trust regions radius R_i is updated at each iteration to make sure that the surrogate function can be trusted. In practice it is adjusted so that decreases or increases in the objective function are correctly predicted by the surrogate model:

$$\forall p \in \mathbb{R}^n,\ T(p) \leq 0,\ \frac{f(p) - f(p_0)}{\tilde{f}(p) - \tilde{f}(p_0)} > \frac{1}{4} \tag{52}$$

Guidelines and algorithms about how to update the trust region radius R_i at each iteration can be found in [22, Chapter 4]. Summarized, the optimization algorithm consists of the following steps:

1. Select an initial point p_0.
2. Compute $f(p_0)$, $\nabla f(p_0)$ and $\nabla^2 f(p_0)$
3. Assume: $f(p) \approx \tilde{f}(p) = f(p_0) + \nabla f(p_0)(p - p_0) + \frac{1}{2}(p - p_0)^T \nabla^2 f(p_0)(p - p_0)$

4.a. If $\nabla^2 f(p_0) > 0$ use line search with Newton-like direction ν:

- Find an approximate minimizer α_m of: $\{f(p_0 + \alpha\nu), \alpha \in [0, 1]\}$
- Define $p_1 = p_0 + \alpha_m\nu$

4.b. Else, a trust region method is used to take the step:

- Define $p_1 = argmin\left\{\tilde{f}(p),\ T(p) \leq 0,\ E_i(p) = 0,\ C_j(p) \leq 0\right\}$

5. Iterate steps 2 to 4 until convergence.

A mixed criterion combining change in function value and 1^{st} order optimality, is used to defined convergence. At least one of the conditions of equation (53) needs to be fulfilled for convergence to be achieved:

$$\begin{cases} \|\hat{\nabla} f(p_0)\| \leq \epsilon_1 \\ |p_k - p_{k+1}| \leq \epsilon_2 \end{cases} \tag{53}$$

In equation (53), $\hat{\nabla}$ is the effective gradient that accounts for equality constraints and active inequality constraint. ϵ_1 is the first order optimality tolerance and ϵ_2 is the step size tolerance. These two parameters should be set by the user. Lastly, it should be noted that the proposed algorithm can still be used when the equality constraints E_i are not linear or the inequality constraints C_j non-convex. In that case, step 4.b. should be used whether the matrix $\nabla^2 f(p_0)$ is positive or not as line search methods are not valid for this type of optimization problems.

5. Examples

In this Section, the algorithm of Section 4 is used in the WFEM Framework with derivatives computed according to Section 2 and 3. Additionally, the complexity of the proposed examples is limited to avoid introducing reduced order modeling considerations or shape optimization formalism. First, the proposed method is used in a FRF-based parameter identification procedure. This serves as a proof of concept and a validation of the implementation. The method is subsequently used to optimize the vibro-acoustic performance of two resonant metabeams. Finally, the optimization of the transmission loss of a metapanel in the coincidence region is considered.

5.1. FRF based parameter identification

In this subsection the method is used in a parameter identification scheme to validate its implementation. A 0.5 meter long beam with a 1cm by 3cm rectangular cross-section and unknown material properties is considered. Assuming a Poisson's ratio of 0.3, the cross section of a beam with unitary density ρ and unitary Young's modulus E is modeled with 108 SOLID 185 elements in ANSYS APDL 17.0 to serve as the basis for a parametric model. The corresponding UC is shown in Figure 3. The mass matrix M_0 and stiffness matrix K_0 are used in a model for which the density, the real part and the imaginary part of the Young's modulus are the parameters as specified in equation (54).

$$\begin{cases} K(p) = (E_r + iE_i)K_0 \\ M(p) = \rho M(p) \\ p = \begin{bmatrix} E_r \\ E_i \\ \rho \end{bmatrix} \end{cases} \tag{54}$$

Clamped-Free boundary conditions are used and a unit force of 1N is applied at the free end of the beam. The direct

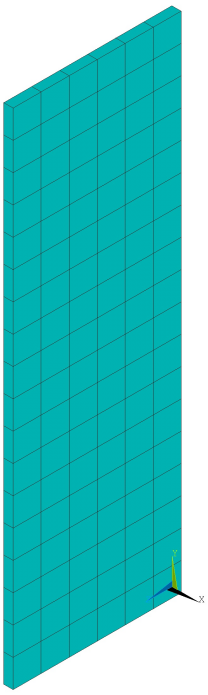

Figure 3: Unit cell for the cross-section of the beam (1cm by 3cm by 0.556mm)

forced response is computed on the 10Hz-1000Hz frequency range for material parameters values corresponding to those of aluminum:

- Real part of the Young's modulus $E_r^0 = 69.10^9 Pa$
- Hysteretic damping $\eta_0 = 0.3\%$
- Imaginary part of the Young's modulus: $E_i^0 = E_r^0 \eta_0 = 2,07.10^9 Pa$
- Density $\rho^0 = 2700 kg.m^{-3}$
- Poisson's ratio $\nu = 0.3$

The response, $X_0(\omega)$, is used to build an error function f that evaluates the difference between the reference and a response obtained using a material property vector p.

$$f(p) = \int_{\omega_-}^{\omega_+} (log(|X_0(\omega)|) - log(|X(\omega, p)|))^2 \, d\omega \tag{55}$$

In equation (55) the logarithm ensures that the objective function is sensitive to the information available on the full frequency range. Without this precaution, modal frequencies would dominate the error evaluation as these are where most of the signal's energy is located. The optimization process is started with material properties $\rho = 13000 kg.m^{-3}$,

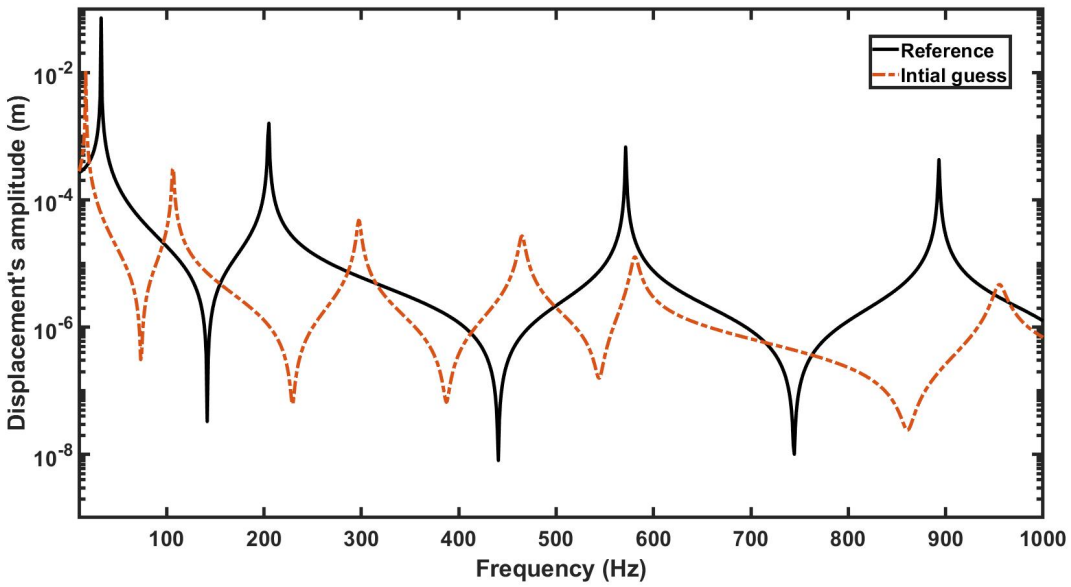

Figure 4: Comparison of the direct forced responses for the reference values and their initial estimates

$E_r = 90.10^9 Pa$ and $E_i = 1,08.10^9 Pa$. The first order optimality tolerance, ϵ_1, is set to 10^{-3} and the step size tolerance, ϵ_2, to 10^{-6}. Additionally, all material properties are constrained to be positive during the optimization process. The difference between the reference forced response and that obtained with the initial guess of the material properties is showcased in Figure 4 while Figure 5 shows the parameter values at each step of the optimization along with the value of the objective function. Looking at the optimization path of the real part of the Young's modulus, iterations 1 and 7 particularly stand out as the value of the real part of the Young's modulus becomes very low. To investigate this, the forced responses for iterations 1, 7, 9 and 11 are displayed in Figure 6. From iterations 1 to 10 the values of the material properties are adjusted so that the average logarithmic values of the forced response match that of the reference case. This explains the very high values for the imaginary part of the Young's modulus and the low values for its real part. Once the mean values approximately correspond, the estimated material properties evolve so that the modal features of the parametric model start matching that of the reference as evidenced from the forced response for iteration 11. Ultimately, the optimization algorithm converges to the reference values of the material properties despite the initial guess being quite off. This constitutes a proof of concept for the method and a validation of its implementation.

5.2. optimization of a resonant metabeam

In this subsection, the wave-based methodology is applied to the optimization of the mean square velocity of a 1m long aluminum beam with a square section of side length 1cm and Clamped-Free boundary conditions. The beam is modeled using Euler-Bernoulli elements and is subjected to a 1N force applied on its free side. The resonant add-on is

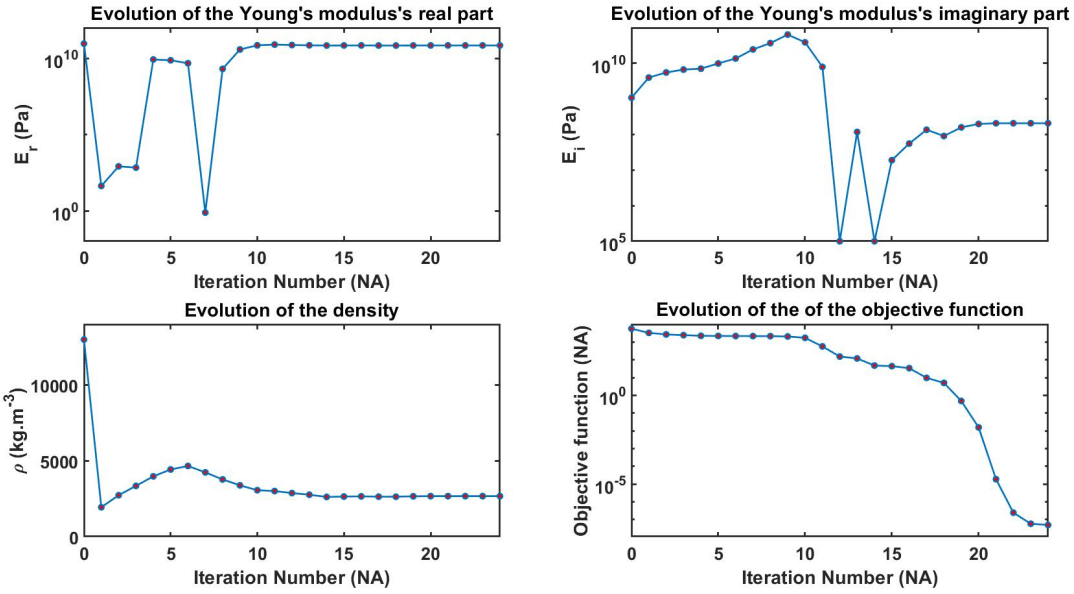

Figure 5: Evolution the objective function and of the material properties' estimates

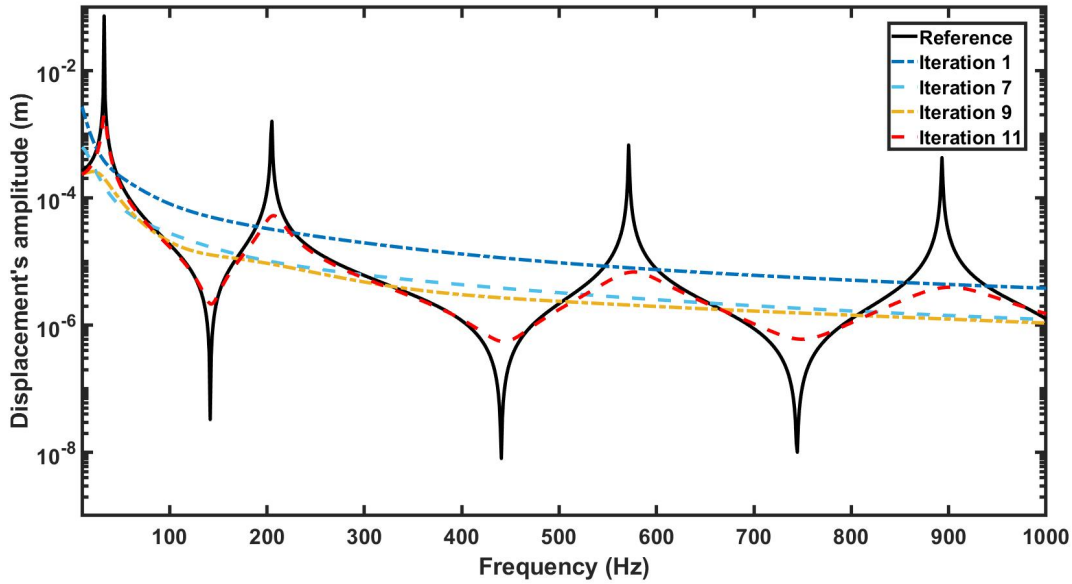

Figure 6: Evolution of the direct forced response's shape through the iterations

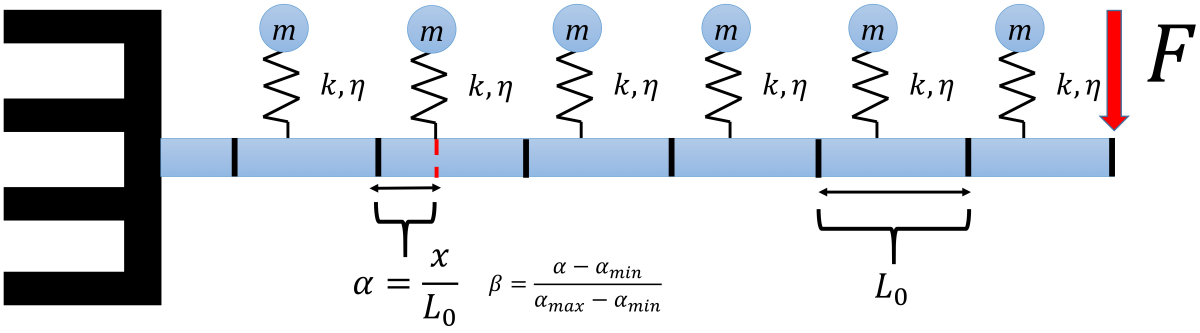

Figure 7: Schematic representation of the metabeam and its parameters

modeled by introducing an additional degree of freedom corresponding to the mass and linked to the corresponding out of plane dof of the bare structure via a spring element. The optimization variables are the mass, stiffness and damping parameters of the periodic resonant add-ons used to treat the host structure. The length of the UC is decided beforehand and fixed to 5cm, hence the beam contains 20 UCs. The variables of the vector of parameters are subsequently introduced:

- The added mass to the UC m (cannot be negative and shall not exceed 20% of the host structure's).
- The stiffness of the spring k (cannot be negative).
- The hystertic damping loss facor of the spring $\eta \in [0\ ,\ 0.1]$.
- The position of the resonator in the UC (should be between 5mm and 4.5cm). The corresponding optimization variable β is normalized to be in the [0 ,1] interval.

Thus the vector of parameters is given in equation (56) while Figure 7 provides a schematic representation of the beam and its parameters:

$$p = \begin{bmatrix} k & \eta & m & \beta \end{bmatrix}^T \tag{56}$$

The objective function takes the form:

$$f(p) = \int_{\omega^-}^{\omega^-} \frac{1}{N} \sum_{i=1}^{N} \omega^2 \, |X_i(p,\omega)|^2 \, d\omega \tag{57}$$

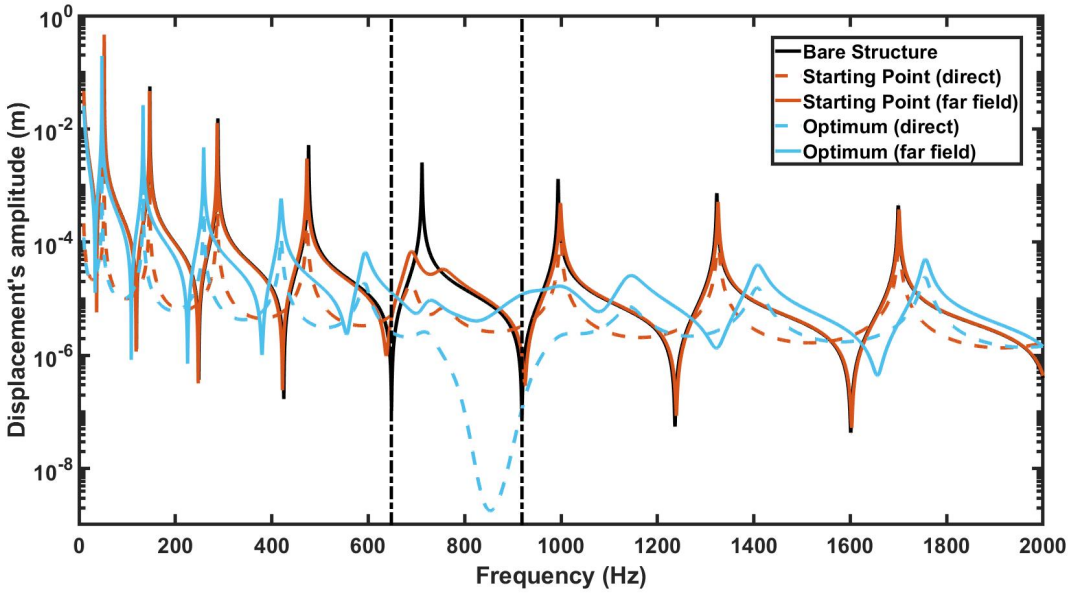

Figure 8: Response of the bare structure (direct), starting point (direct and far field) and optimum (direct and far field). The vertical dashed lines indicate the frequency band of optimization

Where $X_i(p,\omega)$ is the frequency forced response of the i^{th} section of the waveguide for a unitary load on the free side and N is the number of UCs. From a geometric point of view, moving the resonator e.g. to the right can be accomplished by lengthening the elements to its left and shortening the elements to its right by an equal amount. Therefore, the computation of derivatives with respect to β involves the matrix derivatives of Euler-Bernoulli elements with respect to their length. However, when evaluating models with different resonator positions, elements are not lengthened resp. shortened as it would lead to high length ratios between elements when the resonator approaches one of the UCs end. Instead, for a given resonator position, a mesh size is decided according to the shortest distance between the resonator and the UCs ends and re-meshing occurs at each iteration. For the optimization, the 5^{th} mode of the bare structure around 712Hz is targeted as shown in Figure 8. The frequency band of optimization, 648Hz-919Hz, is defined by the two anti-resonances surrounding the 5^{th} mode in the direct forced response of the bare structure. The second order optimization methodology described in Section 4 is applied for a random starting point p_0. The first order optimality tolerance ϵ_1 and the step size tolerance ϵ_2 are set respectively to 10^{-5} and 10^{-6}. In Figure 8, the direct forced response for the bare structure, the starting point of the optimization, and the optimum are shown. Additionally, the response at section 1 (near the clamped side) is presented for the starting point and the optimum so that the stopband behavior can be evaluated in both cases. The value of the optimization variables at each iteration can be observed in Figure 9 while Figure10 shows the evolution of the objective function. Unsurprisingly, maximizing the added mass and loss factor results in optimal performances. However, having the tuned resonance frequency on the targeted mode or at the center of the targeted frequency band does not. Similarly, the resonators position in the

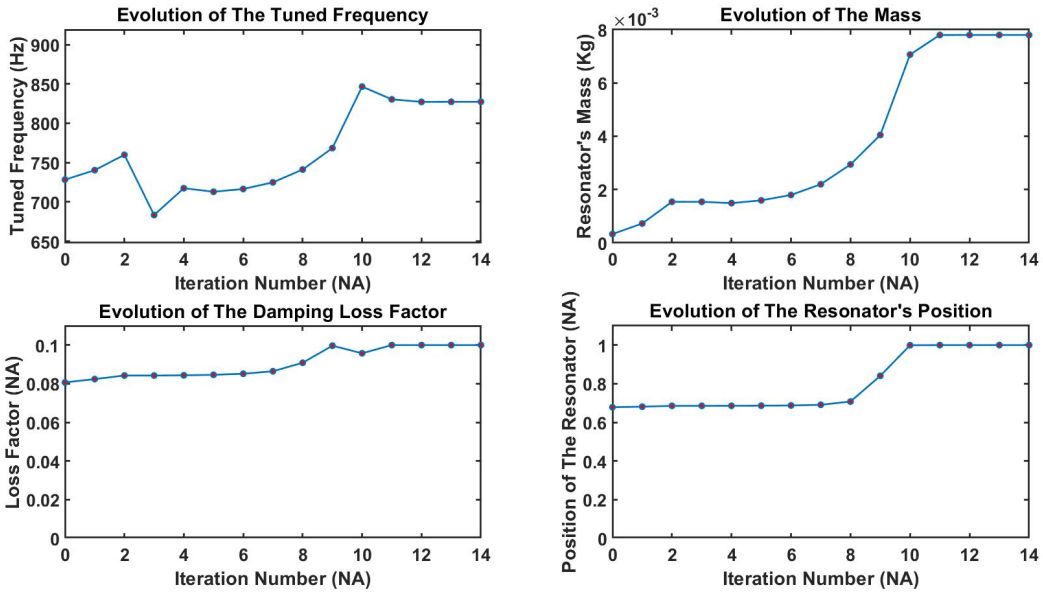

Figure 9: Evolution of the resonator's tuned frequency, mass, damping ratio and position

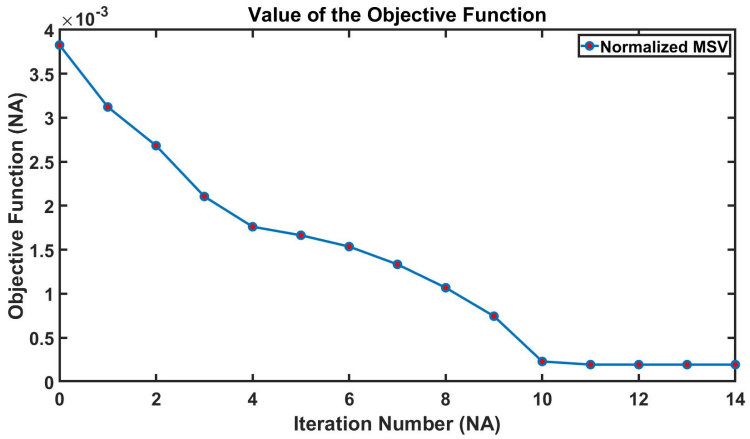

Figure 10: Evolution of the objective function

UC is not a neutral parameter. These observations cannot be predicted from simple dispersion analysis and highlight the need to account for boundary conditions, finiteness and source location properties during the design phase.

5.3. optimization of a multi-resonant metabeam

Given the vibration attenuation obtained in subsection 5.2 the case of multi resonant systems is investigated to see if it is possible to target several modes simultaneously without increasing the percentage of added mass. A 15 cm long UC with 3 resonators is considered. The resonator's positions are fixed at 4.5cm of their respective 5cm long sub-UCs. The length of the beam is also extended to 1.5m as to be a multiple of the 15cm long triple UC and Clamped-Free boundary conditions are used. The targeted frequency band, 188Hz-408Hz is defined by the anti-resonances surrounding the 4th and 5th modes of the host structure. As in the previous case, the added mass of each resonator is limited to 20% of that of the host structure in its sub UC. The damping loss factors are also limited to 10%. The vector of material properties is given in equation (58):

$$p = \begin{bmatrix} k_1 & \eta_1 & m_1 & k_2 & \eta_2 & m_2 & k_3 & \eta_3 & m_3 \end{bmatrix}^T \tag{58}$$

Likewise, the objective function is still that of equation (57):

$$f(p) = \int_{\omega^-}^{\omega^-} \frac{1}{N} \sum_{i=1}^{N} \omega^2 \left| X_i(p,\omega) \right|^2 d\omega$$

The starting point of the optimization is chosen randomly with the additional constraint that all three resonators have identical material properties to see if this still holds for the optimum and during the optimization process. The values of the convergence criteria are set to 10^{-4} for the first order optimality tolerance and 10^{-7} for the step size tolerance. In Figure 11, the direct forced response for the bare structure, the starting point of the optimization, and the optimum are shown. Additionally, the response at section 1 (near the clamped side) is presented for the starting point and the optimum so that the stopband behavior can be evaluated in both cases. The values of the resonators' attributes at each iteration can be observed in Figure 12 along with that of the objective function. The optimum is not really surprising. The added mass and damping loss factor of all resonators reached the maximal allowed values and the tuned resonance frequencies are spread over the optimization zone in order to cover the maximum area.

5.4. Optimization of the diffuse field transmission loss of a resonant metapanel

In this subsection, the 2D WFEM framework is used in conjunction with the method developed by Christen et al. [34] to evaluate and optimize the transmission loss through a metapanel. The general lines of the transmission loss computation are discussed in subsection 5.4.1 in order to introduce the objective function. Then, the modeling of the panel, its parameters and the optimization results are subsequently discussed in subsection 5.4.2.

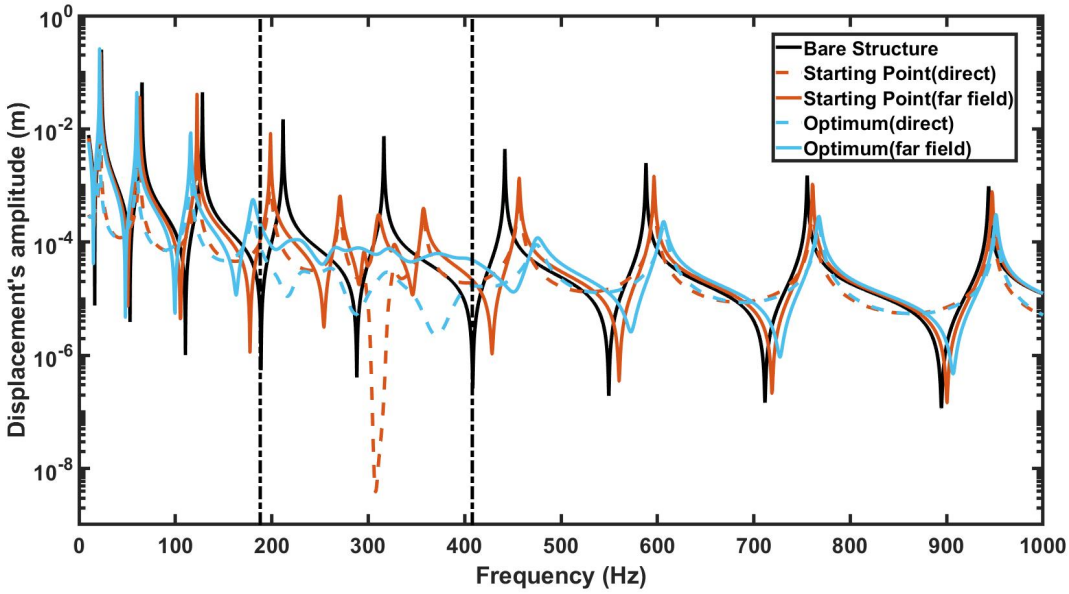

Figure 11: Response of the bare structure (direct), starting point (direct and far field) and optimum (direct and far field). The vertical dashed lines indicate the frequency band of optimization

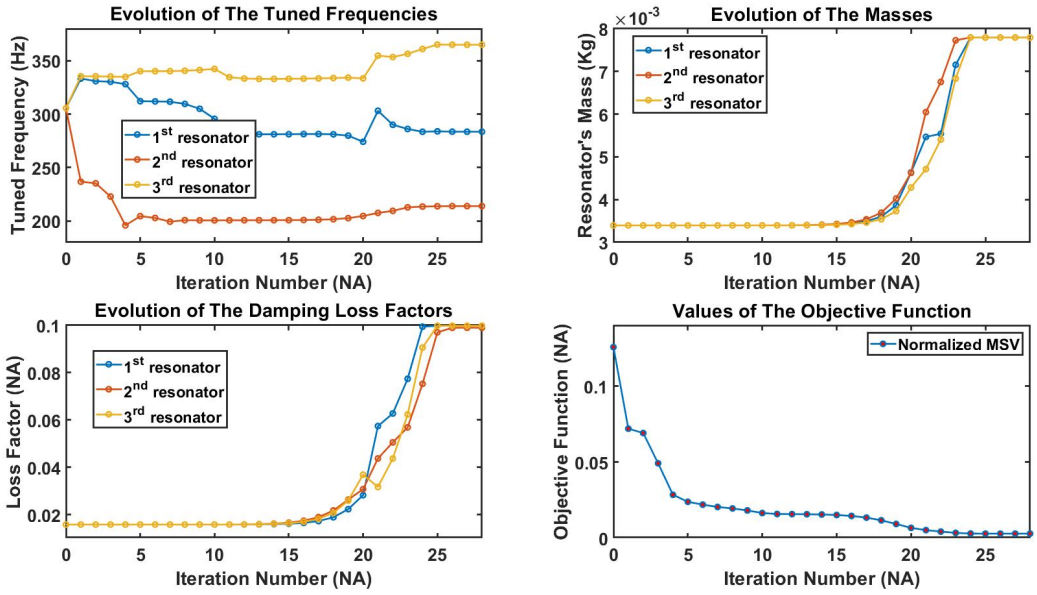

Figure 12: Evolution of the objective function and all three resonators' properties

5.4.1. Transmission loss through a weakly periodic structure

Two semi-infinite acoustic domains separated by a periodic structure filling the space region $-h \leq z \leq 0$ are considered. An incident acoustic field is present in the half space $z \leq -h$ which, by fluid structure coupling, leads to a structural response X, a reflected acoustic field and a transmitted acoustic field. The transmission loss is defined as the ratio between the intensity of the incident field and that of the transmitted one. In 2016, Christen et al. introduced a method based on the 2D WFEM to compute the transmission loss through homogeneous multi-layer panels [34]. The method can be extended to periodic structures assuming that the dimensions of the UC are smaller than all acoustic wavelengths considered and that the structural response to a spatially harmonic load is approximately spatially harmonic. That is, the UC must be subwavelength and the structure weakly periodic. First, the transmission loss for an incident acoustic plane wave at circular frequency ω, acoustic wavenumber k_0 and incidence angles (θ, ϕ) is considered. Using the complex notation, the plane wave has the form:

$$\begin{cases} P_{inc} = P_i e^{-ik_z z} e^{-ik_y y} e^{-ik_x x} \\ k_z = k_0 \cos\phi, \quad k_y = k_0 \sin\theta \sin\phi, \quad k_x = k_0 \cos\theta \sin\phi \end{cases} \tag{59}$$

Its transmission loss, $\tau(\omega, \theta, \phi)$, can be computed by linking the structural displacement to the transmitted and reflected acoustic pressures. Indeed, the continuity of the normal velocity should hold at the two fluid-structure interfaces:

$$\frac{\partial v}{\partial t} = -\frac{\nabla P}{\rho_{air}} \tag{60}$$

In equation (60) P is the pressure on the fluid domain, v is the particle velocity and ρ_{air} is the density of the air. Taking both the spatial and temporal Fourier transforms this equation can be written on both fluid-structure interfaces:

$$P_r = P_i - \frac{i\rho_{air}\omega^2}{k_z} X_- \tag{61}$$

$$P_t = \frac{i\rho_{air}\omega^2}{k_z} X_+ \tag{62}$$

with X_- the out of plane structural displacement at the incident side and X_+ the out of plane displacement at the transmission side. The reflected and transmitted pressure fields take the form:

$$\begin{cases} P_{ref} = P_r e^{ik_z z} e^{-ik_y y} e^{-ik_x x} \\ P_{tra} = P_t e^{-ik_z z} e^{-ik_y y} e^{-ik_x x} \end{cases} \tag{63}$$

Following the logic of Section 3.1, the complete structural response X can be evaluated by solving:

$$\left(D(k_x, k_y) + A^+(k_z) + A^-(k_z)\right) X = 2F_i \tag{64}$$

In equation (64), F_i is the force vector associated to the incident pressure field while $A^+(k_z)$ and $A^-(k_z)$ integrate the parts of the reflected and transmitted pressure fields that scale linearly with the structural displacement. The factor 2 comes from the fact that the reflected pressure is derived from both the displacement and the incident pressure. Once the structural displacement is known, the quadratic amplitude of transmitted pressure field can be evaluated:

$$|P_t|^2 = \frac{\rho_{air}\omega^2}{N k_z} X_+^* X_+ \tag{65}$$

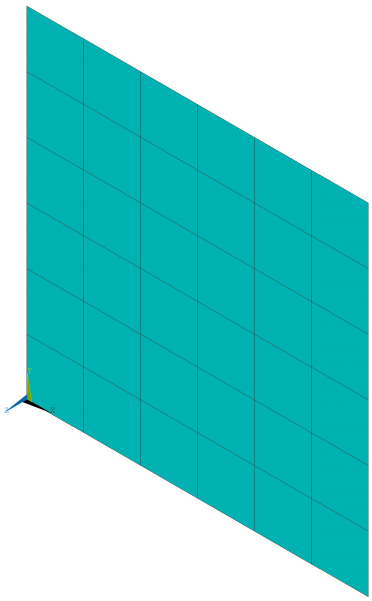

Figure 13: Unit Cell of the host structure

With X_+ the structural displacement at the interface and N the dimension of X_+. The transmission loss $\tau(\omega, \theta, \phi)$ is then defined as:

$$\tau(\omega, \theta, \phi) = \frac{|P_t|^2}{|P_i|^2} \tag{66}$$

The diffuse transmission loss at the circular frequency ω can then be obtained as:

$$\tau_d(\omega) = \frac{\int_0^{2\pi} \int_0^{\frac{\pi}{2}} \tau(\omega, \theta, \phi) \sin\theta \cos\theta \, d\theta \, d\phi}{\int_0^{2\pi} \int_0^{\frac{\pi}{2}} \sin\theta \cos\theta \, d\theta \, d\phi} \tag{67}$$

while the global diffuse field transmission loss on the frequency range $[\omega_-, \omega_+]$ is defined by:

$$\tau_g(\omega^-, \omega^+) = \frac{\int_0^{2\pi} \int_0^{\frac{\pi}{2}} \int_{\omega-}^{\omega_+} \tau(\omega, \theta, \phi) \sin\theta \cos\theta \, d\theta \, d\phi \, d\omega}{\int_0^{2\pi} \int_0^{\frac{\pi}{2}} \int_{\omega-}^{\omega_+} \sin\theta \cos\theta \, d\theta \, d\phi \, d\omega} \tag{68}$$

Finally, while the present section maintained the distinction between X_+ and X_- (in accordance to [34]) these vectors are equal in subsection 5.4.2 because shell elements are used to model the metapanel.

5.4.2. Numerical modeling and results

The method described in subsection 5.4.1 is applied to a metapanel. The bare panel is 4 mm thick and mass spring systems are added to it periodically. The UC is chosen to be 1cm by 1cm which guarantees that the subwavelength condition is respected. The host structure's UC is modeled in Ansys APDL 17.0 with elements SHELL181. Its mesh is shown in Figure 13. The additional dof of the mass is connected to the central node of the UC and the parameters of

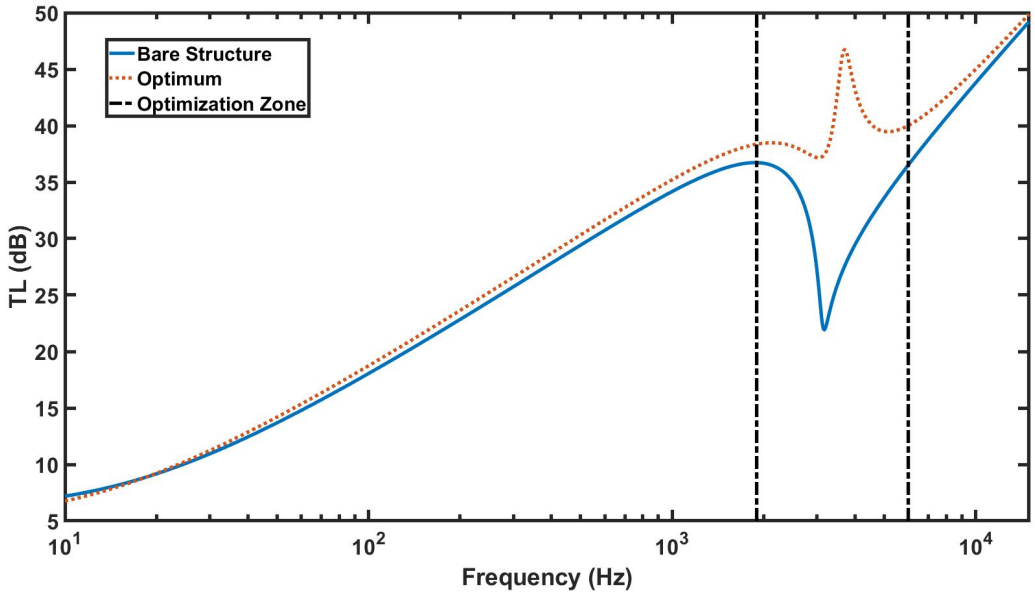

Figure 14: Comparison of the performance of the host structure and the optimum

the model are the added mass, the stiffness of the spring and the hysteretic damping. The mass is constrained so that it does not exceed 10% of the host structure's mass while the damping is limited to 10%. The parameter vector is:

$$p = \begin{bmatrix} k \\ \eta \\ m \end{bmatrix} \tag{69}$$

The aim of the optimization is to mitigate the decrease of transmission loss in the 1900-6000 Hz frequency range caused by the structural-acoustic coincidence (see Figure 14) hence the objective function is:

$$f(p) = \frac{\int_0^{2\pi} \int_0^{\frac{\pi}{2}} \int_{\omega-}^{\omega+} \tau(\omega, \theta, \phi, p) \sin\theta \cos\theta \, d\theta \, d\phi \, d\omega}{\int_0^{2\pi} \int_0^{\frac{\pi}{2}} \int_{\omega-}^{\omega+} \sin\theta \cos\theta \, d\theta \, d\phi \, d\omega} \tag{70}$$

where $\tau(\omega, \theta, \phi, p)$ is the transmission loss for an incident acoustic wave at circular frequency ω and angles (θ, ϕ) and parameter vector p. This function satisfies the conditions of Appendix A.2 (see equation (66)), therefore the additional cost of computing its derivatives is low. The optimization is carried out starting from a random point in the design space with stopping criteria values set to 10^{-16} for the first order optimality tolerance and 10^{-7} for the minimal step size. A comparison between the TL of the bare structure and that of the optimal design is given in Figure 14. Additionally, Figure 15 shows the optimization path of the resonators attributes as well as the value of the objective function. As expected, maximizing the TL requires to maximize both the mass and damping of the resonator and the optimal tuned frequency is close to that of the minimal TL for the bare structure. The optimum is reached in a few iterations despite the starting point being far from the optimal values, proving the efficiency of the optimization methodology.

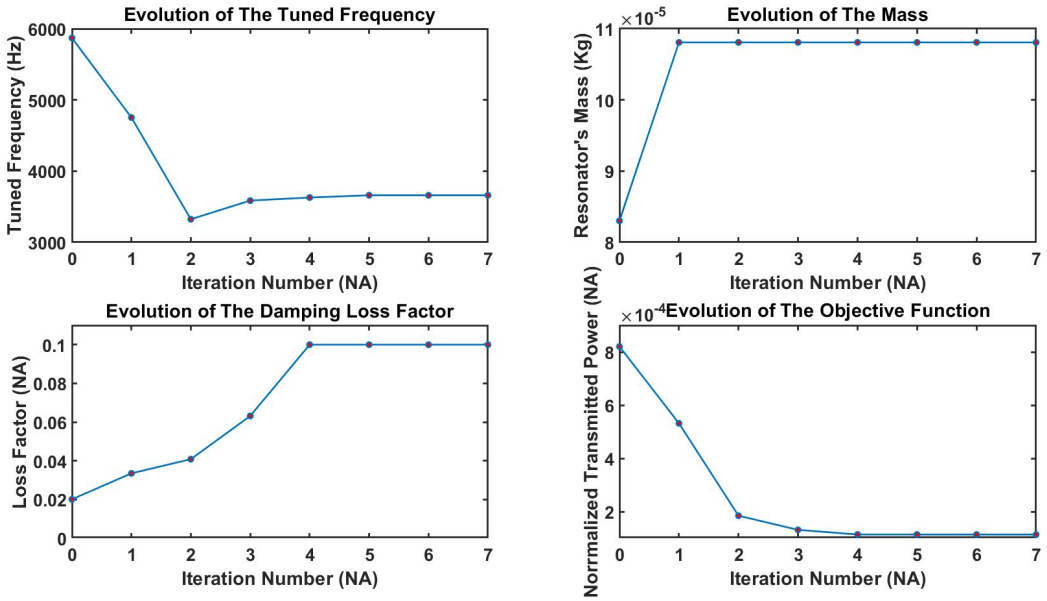

Figure 15: Evolution of the objective function and of the TVA's properties

6. Conclusion

In this paper, first and second order derivatives were derived for the 1D and 2D WFEM via an intrusive methodology. Additionally, a second order optimization algorithm belonging to the class of sequential quadratic programming was proposed to exploit the derivatives to their fullest. This algorithm combines an ellipsoidal trust-region approach with a line search method when appropriate. When it is not, the algorithm reduces to a trust region method. Combined, both contributions form a framework for the optimization of 1D and 2D periodic structures. In the 1D case, the size of the waveguide, the boundary conditions and eventual loads can all be taken into account during the optimization process. In the 2D case, only infinite structures are considered but the load's characteristics can still be accounted for. This is demonstrated in the numerical examples in which the proposed methodology is used to successfully optimize the vibro-acoustic performances of metabeams under clamped-free boundary conditions and the diffuse field transmission loss of a metapanel. The proposed methodology accounts for both strong and weak points of the WFEM. Namely, the decoupling of the computation cost from the size of the waveguide and the lower accuracy of the WFEM as compared to FEM modeling. It is versatile and can be used in a wide range of applications including parameter identification, homogenization, model updating, design optimization and potentially damage detection. Further technical developments will focus on the incorporation of model order reduction in the proposed framework and its extension to other UCM techniques such as the shift cell operator method. The former could prove challenging because rigorously, the sensibilities of projection matrices are required to ensure the accuracy of the gradient and Hessian matrix of objective functions. Finally, applications with complex cases including 3D geometric parameters will be considered.

Acknowledgements

The research of R. F. Boukadia is funded by an Early Stage Researcher grant within the European Project VIPER Marie Curie Initial Training Network (GA 675441). The research of E. Deckers is funded by a grant from the Research Foundation Flanders (FWO). This research is partially supported by Flanders Make, the strategic research centre for the manufacturing industry.

Appendix A. First and second order derivatives for solutions of linear equations

This section details the computation of first of second order derivatives for functions using solutions of linear systems of equations. This is relevant to the developments in subsections 2.1, 3.1 and 5.4. A C^2 linear parametric system is considered:

$$A(p)U(p) = F \tag{A.1}$$

In equation (A.1), $p \in \mathbb{R}^n$ is the vector of parameters. Appendix A.1 deals with the derivative of the vector function U while Appendix A.2 describes an efficient way to compute the gradient and hessian of a scalar quadratic objective function based on U

Appendix A.1. Vector Derivatives

The solution of equation (A.1) can be written:

$$U = A^{-1}F \tag{A.2}$$

Practically, solving equation (A.1) numerically involves the computation of a decomposition of the matrix A which may depend on its properties (LU, LDL, Cholesky, QR, etc). This decomposition should be stored as inverting A again will be needed to compute the derivatives of U. Indeed differentiating equation (A.1) yields:

$$\frac{\partial A}{\partial p_i}U + A\frac{\partial U}{\partial p_i} = 0 \tag{A.3}$$

Hence:

$$\frac{\partial U}{\partial p_i} = -A^{-1}\frac{\partial A}{\partial p_i}U \tag{A.4}$$

The same can be done for the second order derivatives U.

$$\frac{\partial^2 U}{\partial p_i \partial p_j} = -A^{-1}\left(\frac{\partial^2 A}{\partial p_i \partial p_j}U + \frac{\partial A}{\partial p_i}\frac{\partial U}{\partial p_j} + \frac{\partial A}{\partial p_j}\frac{\partial U}{\partial p_i}\right) \tag{A.5}$$

Since A^{-1} is used in equations (A.2), (A.4) and (A.5), keeping the matrix decomposition of A enables the computation of the first of second order derivatives of U at a relatively low cost.

Appendix A.2. Scalar Derivatives

For this case, the solution of equation (A.1) is used in a scalar objective function $f(p)$ and the aim is to compute the gradient and hessian of this function in a efficient manner. In light of the objective functions used in this article we will focus on quadratic implicit vector functions corresponding to the system of equations (A.6).

$$\begin{cases} A(p)U(p) = F \\ f(p) = U^*BU \end{cases} \tag{A.6}$$

In (A.6) the matrix B can be chosen hermitian without loss of generality hence this assumption will be made in the following developments. First, the first order derivatives of f are introduced:

$$\frac{\partial f}{\partial p_i} = 2\Re\left(U^*B\frac{\partial U}{\partial p_i}\right) \tag{A.7}$$

Then, the derivatives of U can be replaced using equation (A.4):

$$\frac{\partial f}{\partial p_i} = 2\Re\left(-U^*BA^{-1}\frac{\partial A}{\partial p_i}U\right) = 2\Re\left((-U^*BA^{-1})\left(\frac{\partial A}{\partial p_i}U\right)\right) \tag{A.8}$$

Equation (A.8) introduces the adjoint:

$$Adj = -U^*BA^{-1} = -(U^*B)A^{-1} \tag{A.9}$$

It needs only to be computed once at the cost of one matrix-vector inversion. Then, all first order derivatives of f can be computed at the cost of one matrix-vector multiplication and one vector-vector scalar product. This significantly lowers the computation cost of f's gradient. The second order derivatives of f are given by:

$$\frac{\partial^2 f}{\partial p_i \partial p_j} = 2\Re\left(U^*B\frac{\partial^2 U}{\partial p_i \partial p_j} + \frac{\partial U^*}{\partial p_i}B\frac{\partial U}{\partial p_j}\right) \tag{A.10}$$

Using equations (A.5) and (A.9) this can rewritten as:

$$\frac{\partial^2 f}{\partial p_i \partial p_j} = 2\Re\left(Adj\left(\frac{\partial^2 A}{\partial p_i \partial p_j}U + \frac{\partial A}{\partial p_i}\frac{\partial U}{\partial p_j} + \frac{\partial A}{\partial p_j}\frac{\partial U}{\partial p_i}\right) + \frac{\partial U^*}{\partial p_i}B\frac{\partial U}{\partial p_j}\right) \tag{A.11}$$

Unlike equation (A.10), equation (A.11) does not involve $\frac{\partial^2 U}{\partial p_i \partial p_j}$: This means that the full hessian matrix of f can be computed at the cost of only $(n+1)$ matrix inversions instead of $\frac{n(n+3)}{2}+1$. However, since both equation (A.10) and (A.11) require the first order derivatives of U it is not necessary to use equations (A.8) and (A.9) to compute f's gradient as equation (A.7) is equally fast under these conditions. That being said, using equation (A.8) never result in a loss of computation time.

Appendix B. Derivatives of Simple Eigenvalues and Eigenvectors

This section is concerned with the first and second order derivatives of eigenvalues and eigenvectors. In order increase readability, the following notations are introduced:

- U/U_i : Right eigenvector.
- V/V_i : Left eigenvector.
- λ/λ_i : Eigenvalue, propagation constant.
- $p \in \mathbb{R}^m$ vector of parameters.
- p_i The i^{th} component of p.
- X^+ Moore-Penrose inverse of the matrix X.

Appendix B.1. Nonlinear Eigenvalue Problem

Let m be a positive integer superior or equal to 1. A nonlinear eigenvalue problem of order n is defined by the following equation:

$$\begin{cases} X : \mathbb{C} \to M_n(\mathbb{C}) \\ \lambda \mapsto X(\lambda) \\ Sol = \{\lambda \in \mathbb{C}, det(X(\lambda)) = 0\} \end{cases} \tag{B.1}$$

For each λ in Sol left and right eigenvectors can be defined. They are non-trivial solutions of equation (B.2):

$$X(\lambda)U = 0 = V^T X(\lambda) \tag{B.2}$$

For a given λ in Sol, the dimension of $Ker(X(\lambda))$ is at least one. Herein, the assumption that $Ker(X(\lambda))$ (the kernel of $X(\lambda)$) is always of dimension 1 is made. In this case, single left and right eigenvectors can be arbitrarily chosen as all possible choices differ only by a scalar multiplication.

Appendix B.2. Parametric Eigenvalue Problem

This time the matrix X is considered to also be a function of a parameter vector $p \in \mathbb{R}^m$. The eigenvalues λ and eigenvectors U and V become function of p. Assuming the matrix X is an analytic function of (λ, p), derivatives of eigenvalues and eigenvectors with respect to the parameters p_i can be computed. In order to simplify expressions we define:

$$\frac{dX}{dp_k} = \frac{\partial X}{\partial p_k} + \frac{\partial \lambda}{\partial p_k}\frac{\partial X}{\partial \lambda} \tag{B.3}$$

Appendix B.2.1. First Order Derivatives

An arbitrary eigenvalue λ_i and the corresponding left and right eigenvectors U_i and V_i are chosen. The relationship (B.4) holds:

$$\forall p \in \mathbb{R}^m, X(\lambda_i(p), p)U_i(p) = 0 = V_i^T(p)X(\lambda_i(p), p) \tag{B.4}$$

Differentiating with respect to p_k we get:

$$\frac{dX}{dp_k}U_i + X\frac{\partial U_i}{\partial p_k} = 0 \tag{B.5}$$

Since $V_i^T X = 0$, premultiplying by V_i^T yields:

$$V_i^T \frac{dX}{dp_k} U_i = 0 \tag{B.6}$$

This scalar equation can be developed using equation (B.3):

$$\frac{\partial \lambda}{\partial p_k}\left(V_i^T \frac{\partial X}{\partial \lambda} U_i\right) = -\left(V_i^T \frac{\partial X}{\partial p_k} U_i\right) \tag{B.7}$$

Equation (B.7) defines the first order derivatives of the eigenvalue λ_i. Once this quantity is known, equation (B.3) can be evaluated and the derivatives of the eigenvectors can be obtained:

$$\frac{\partial U_i}{\partial p_k} = -X^+ \frac{dX}{dp_k} U_i \tag{B.8}$$

Since the matrix X is singular, there would be infinitely many solutions to equation (B.8) if the Moore-Penrose inverse was not used. This corresponds to a choice of normalized rectified eigenvectors satisfying $\left(\frac{dU_i}{dp_k}\middle| U_i\right) = 0$. This condition can be enforced without making any particular hypothesis (see Appendix B.3).

Appendix B.2.2. Second Order Derivatives

It is assumed that the first order derivatives of eigenvalues and eigenvectors have been computed and stored in memory. Differentiating equation (B.2) two times provides:

$$\frac{d^2X}{dp_k dp_l} U + \frac{dX}{dp_k}\frac{\partial U}{\partial p_l} + \frac{dX}{dp_l}\frac{\partial U}{\partial p_k} + X\frac{\partial^2 U}{\partial p_k \partial p_l} = 0 \tag{B.9}$$

Since $V^T X = 0$, premultiplying by V^T yields:

$$V^T\left(\frac{d^2X}{dp_k dp_l} U + \frac{dX}{dp_k}\frac{\partial U}{\partial p_l} + \frac{dX}{dp_l}\frac{\partial U}{\partial p_k}\right) = 0 \tag{B.10}$$

The term $\frac{d^2X}{dp_k dp_l}$ can be developed leading to the expression for the second order derivatives of λ:

$$\frac{d^2\lambda}{\partial p_k \partial p_l}\left(V^T \frac{\partial X}{\partial \lambda} U\right) = -V^T\left[\left(\frac{\partial^2 X}{\partial p_l \partial p_k} + \frac{\partial \lambda}{\partial p_l}\frac{\partial^2 X}{\partial \lambda \partial p_k} + \frac{\partial \lambda}{\partial p_k}\frac{\partial^2 X}{\partial \lambda \partial p_l} + \frac{\partial \lambda}{\partial p_k}\frac{\partial \lambda}{\partial p_l}\frac{\partial^2 X}{\partial \lambda^2}\right) U + \left(\frac{dX}{dp_k}\frac{dU}{dp_l} + \frac{dX}{dp_l}\frac{dU}{dp_k}\right)\right] \tag{B.11}$$

Once that $\frac{d^2\lambda}{\partial p_k \partial p_l}$ is known, the matrix $\frac{d^2X}{dp_k d_p l}$ can be evaluated and the second order derivatives of the eigenvector can be obtained:

$$\frac{\partial^2 U}{\partial p_l \partial p_k} = -X^+\left(\frac{d^2X}{dp_k dp_l} U + \frac{dX}{dp_k}\frac{\partial U}{\partial p_l} + \frac{dX}{dp_l}\frac{\partial U}{\partial p_k}\right) - \Re\left(\left(\frac{\partial U}{\partial p_l}\middle|\frac{\partial U}{\partial p_k}\right)\right) U \tag{B.12}$$

For explanations about formula (B.12) see Appendix B.3

Appendix B.3. Proofs

The aim of this subsection is to determines how equation of the form:

$$XA = B \tag{B.13}$$

Should be solved in the context of eigenvector derivatives computations. Indeed, equations (B.5) and (B.9) can be used to evaluate the derivatives of the eigenvector. However, because the matrix function is singular when λ is an

eigenvalue, an infinite number of solutions exists. This subsection shows that solving according to equation (B.14) produces a coherent set of derivatives.

$$\begin{cases} \left(U_i(p)\middle|\dfrac{\partial U_i(p)}{\partial p_k}\right) = 0 \\ \left(U_i(p)\middle|\dfrac{\partial^2 U_i(p)}{\partial p_k \partial p_l}\right) = -\Re\left(\left(\dfrac{\partial U_i(p)}{\partial p_k}\middle|\dfrac{\partial U_i(p)}{\partial p_l}\right)\right) \end{cases} \tag{B.14}$$

In what follows, it is assumed that the derivatives are computed for $p = 0$ and that they are C^2 functions of the eigenvalue λ_i and the eigenvectors U_i. We start by normalizing the eigenvector function. That is, we use $\frac{1}{\|U_i(p)\|}U_i(p)$ instead of $U_i(p)$. Since eigenvectors are defined up to a multiplicative constant this function is still ane eigenvector function. Moreover it is also C^2 since U_i cannot be equal to zero (eigenvectors are non-trivial solutions). In what follows we still note this new function $U_i(p)$.

$$\forall p \in \mathbb{R}^m,\ \|U_i(p)\| = 1 \tag{B.15}$$

Tatking the first order derivative of equation (B.15) yields

$$\forall p \in \mathbb{R}^m,\ \Re\left(\frac{\partial Ui}{\partial p_k}\middle|U_i\right) = \Re\left(U_i\middle|\frac{\partial Ui}{\partial p_k}\right) = 0 \tag{B.16}$$

Considering the second order derivatives leads to:

$$\forall p \in \mathbb{R}^m,\ \ \Re\left(U_i(p)\middle|\frac{\partial^2 U_i(p)}{\partial p_k \partial p_l}\right) = -\Re\left(\frac{\partial U_i(p)}{\partial p_k}\middle|\frac{\partial U_i(p)}{\partial p_l}\right) \tag{B.17}$$

Equations (B.16) and (B.17) are only true for the imaginary parts because the $(\ |\ )$ is an hermitian inner product. Therefore we still have to show that the imaginary part of the concerned inner products can be chosen equal to 0. Equation (B.16) can be rewritten for $p = 0$ as:

$$\frac{\partial U_i}{\partial p_k}(0) = j\alpha_k U_i(0) + Q_k \tag{B.18}$$

With

$$\forall k\ \in [\![1, m]\!], \alpha_k \in \mathbb{R},\ (U_i(0)|Q_k) = 0,\ j^2 = -1 \tag{B.19}$$

The eigenvector function R defined by equation (B.20) is considered:

$$\forall p, \in \mathbb{R}^m, R_i(p) = U_i(p)e^{-j(\alpha|p)} \tag{B.20}$$

The function R is also a normalized eigenvector function since $\left|e^{-j(\alpha|p)}\right| = 1$ hence, it satisfies equations (B.16) and (B.17). Taking the first order derivatives of R leads to:

$$\frac{\partial R_i}{\partial p_k} = \left(\frac{\partial U_i}{\partial p_k} - j\alpha_k U_i\right)e^{-j(\alpha|p)} \tag{B.21}$$

Therefore:

$$\begin{cases} R(0) = U_i(0)e^{-j(\alpha|0)} = U_i(0) \\ \dfrac{\partial R_i}{\partial p_k}(0) = Q_k e^{-j(\alpha|0)} = Q_k \\ Hence,\ \left(R(0)\middle|\dfrac{\partial R_i}{\partial p_k}(0)\right) = 0 \end{cases} \tag{B.22}$$

The first condition of equation (B.14) is verified by the eigenvector function R_i but not necessarily the second one. It follows that:

$$\begin{cases} \dfrac{\partial^2 R_i}{\partial p_k \partial p_l}(0) = (\beta_{k,l} + j\gamma_{k,l})\, U_i(0) + W_{k,l} \\ \forall (k,l) \in [\![1,m]\!]^2,\ (\beta_{k,l}, \gamma_{k,l}) \in \mathbb{R}^2,\ (R_i(0)\big|W_{k,l}) = 0 \end{cases} \tag{B.23}$$

It should be noted that by Schwartz theorem $\beta_{k,l} = \beta_{l,k}$. The same holds true for $\gamma_{k,l}$ and $W_{k,l}$. The m by m matrix H is defined such that $H_{k,l} = \frac{\gamma_{k,l}}{2}$. H is real symmetric. We can now define the normalized eigenvector function S by:

$$\forall p \in \mathbb{R}^m,\ S_i(p) = R_i(p)e^{-jp^T Hp} \tag{B.24}$$

Let $(\nu_k)_{k\in[\![1,m]\!]}$ be the canonical basis of $\mathbb{R}^m$. We have:

$$\begin{cases} S_i(p) = R_i(p)e^{-jp^T Hp} \\ \dfrac{\partial S_i}{\partial p_k} = \left(\dfrac{\partial R_i}{\partial p_k} - 2j\left(\nu_k^T Hp\right)R_i\right)e^{-jp^T Hp} \\ \dfrac{\partial^2 S_i}{\partial p_l \partial p_k} = \left[-2j\left(\nu_l^T Hp\right)\left(\dfrac{\partial R_i}{\partial p_k} - 2j\left(\nu_k^T Hp\right)R_i\right) + \left(\dfrac{\partial^2 R_i}{\partial p_l \partial p_k} - 2j\left(\nu_k^T H\nu_l\right)R_i - 2j\left(\nu_k^T Hp\right)\dfrac{\partial R_i}{\partial p_l}\right)\right]e^{-jp^T Hp} \end{cases} \tag{B.25}$$

Evaluating these expressions at $p = 0$ yields:

$$\begin{cases} S_i(0) = R_i(0) \\ \dfrac{\partial^2 S_i}{\partial p_k}(0) = \dfrac{\partial R_i}{\partial p_k}(0) \\ \dfrac{\partial^2 S_i}{\partial p_l \partial p_k}(0) = \dfrac{\partial^2 R_i}{\partial p_l \partial p_k}(0) - 2jH_{k,l}R_i(0) = \beta_{k,l}R_i(0) + W_{k,l} \end{cases} \tag{B.26}$$

Hence the eigenvector function S_i satisfies all the conditions of equation (B.14). This proves that the formulas (B.8) and (B.12) produce a coherent system of eigenvector derivatives.

Appendix C. Derivatives of the wave stiffness matrix

This section details computation of the derivatives of the wave stiffness matrix in equations (5) and (20).

$$\begin{cases} W_{11} = \Psi^+ \\ W_{12} = \Psi^-\Lambda^N \\ W_{21} = D_{RL}\Psi^+\Lambda^{N-1} + D_{RR}\Psi^+\Lambda^N \\ W_{22} = D_{RL}\Psi^-\Lambda + D_{RR}\Psi^- \end{cases} \tag{C.1}$$

The derivatives of W_{11} are trivial but that of the other submatrices are developed:

$$\frac{\partial W_{12}}{\partial p_k} = \frac{\partial \Psi^-}{\partial p_k}\Lambda^N + N\Psi^- \frac{\partial \Lambda}{\partial p_k}\Lambda^{N-1} \tag{C.2}$$

$$\frac{\partial^2 W_{12}}{\partial p_k \partial p_l} = \frac{\partial^2 \Psi^+}{\partial p_k \partial p_l}\Lambda^N + N\left(\frac{\partial \Psi^-}{\partial p_k}\frac{\partial \Lambda}{\partial p_l} + \frac{\partial \Psi^-}{\partial p_l}\frac{\partial \Lambda}{\partial p_k} + \Psi^+ \frac{\partial^2 \Lambda}{\partial p_k \partial p_l}\right)\Lambda^{N-1} + N(N-1)\Psi^- \frac{\partial \Lambda}{\partial p_k}\frac{\partial \Lambda}{\partial p_l}\Lambda^{N-2} \tag{C.3}$$

$$\frac{\partial W_{21}}{\partial p_k} = \left(\frac{\partial D_{RL}}{\partial p_k}\Psi^+ + D_{RL}\frac{\partial \Psi^+}{\partial p_k}\right)\Lambda^{N-1} + (N-1)D_{RL}\Psi^+ \frac{\partial \Lambda}{\partial p_k}\Lambda^{N-2} + \left(\frac{\partial D_{RR}}{\partial p_k}\Psi^+ + D_{RR}\frac{\partial \Psi^+}{\partial p_k}\right)\Lambda^N + ND_{RR}\Psi^+ \frac{\partial \Lambda}{\partial p_k}\Lambda^N \tag{C.4}$$

$$\begin{aligned}
\frac{\partial^2 W_{21}}{\partial p_k \partial p_l} =& \left(\frac{\partial^2 D_{RL}}{\partial p_k \partial p_l}\Psi^+ + \frac{\partial D_{RL}}{\partial p_k}\frac{\partial \Psi+}{\partial p_l} + \frac{\partial D_{RL}}{\partial p_l}\frac{\partial \Psi+}{\partial p_k} + D_{RL}\frac{\partial^2 \Psi^+}{\partial p_k \partial p_l}\right)\Lambda^{N-1} \\
&+ (N-1)\left[\left(\frac{\partial D_{RL}}{\partial p_k}\Psi^+ + D_{RL}\frac{\partial \Psi^+}{\partial p_k}\right)\frac{\partial \Lambda}{\partial p_l} + \left(\frac{\partial D_{RL}}{\partial p_l}\Psi^+ + D_{RL}\frac{\partial \Psi^+}{\partial p_l}\right)\frac{\partial \Lambda}{\partial p_k} + D_{RL}\Psi\frac{\partial^2 \Lambda}{\partial p_k \partial p_l}\right]\Lambda^{N-2} \\
&+ (N-1)(N-2)D_{RL}\Psi^+ \frac{\partial \Lambda}{\partial p_k}\frac{\partial \Lambda}{\partial p_l}\Lambda^{N-3} \\
&+ \left(\frac{\partial^2 D_{RR}}{\partial p_k \partial p_l}\Psi^+ + \frac{\partial D_{RR}}{\partial p_k}\frac{\partial \Psi+}{\partial p_l} + \frac{\partial D_{RR}}{\partial p_l}\frac{\partial \Psi+}{\partial p_k} + D_{RR}\frac{\partial^2 \Psi^+}{\partial p_k \partial p_l}\right)\Lambda^N \\
&+ N\left[\left(\frac{\partial D_{RR}}{\partial p_k}\Psi^+ + D_{RR}\frac{\partial \Psi^+}{\partial p_k}\right)\frac{\partial \Lambda}{\partial p_l} + \left(\frac{\partial D_{RR}}{\partial p_l}\Psi^+ + D_{RR}\frac{\partial \Psi^+}{\partial p_l}\right)\frac{\partial \Lambda}{\partial p_k} + D_{RR}\Psi\frac{\partial^2 \Lambda}{\partial p_k \partial p_l}\right]\Lambda^{N-1} \\
&+ N(N-1)D_{RR}\Psi^+ \frac{\partial \Lambda}{\partial p_k}\frac{\partial \Lambda}{\partial p_l}\Lambda^{N-2}
\end{aligned} \tag{C.5}$$

$$\frac{\partial W_{22}}{\partial p_k} = \left(\frac{\partial D_{RL}}{\partial p_k}\Psi^- + D_{RL}\frac{\partial \Psi}{\partial p_k}\right)\Lambda + D_{RL}\Psi^- \frac{\partial \Lambda}{\partial p_k} + \frac{\partial D_{RR}}{\partial p_k}\Psi^- + D_{RR}\frac{\partial \Psi^-}{\partial p_k} \tag{C.6}$$

$$\begin{aligned}
\frac{\partial^2 W_{22}}{\partial p_k \partial p_l} =& \left(\frac{\partial^2 D_{RL}}{\partial p_k \partial p_l}\Psi^- + \frac{\partial D_{RL}}{\partial p_k}\frac{\partial \Psi^-}{\partial p_l} + \frac{\partial D_{RL}}{\partial p_l}\frac{\partial \Psi^-}{\partial p_k} + D_{RL}\frac{\partial^2 \Psi^-}{\partial p_k \partial p_l}\right)\Lambda \\
&+ \left(\frac{\partial D_{RL}}{\partial p_k}\Psi^- + D_{RL}\frac{\partial \Psi^-}{\partial p_k}\right)\frac{\partial \Lambda}{\partial p_l} + \left(\frac{\partial D_{RL}}{\partial p_l}\Psi^- + D_{RL}\frac{\partial \Psi^-}{\partial p_l}\right)\frac{\partial \Lambda}{\partial p_k} + D_{RL}\Psi^- \frac{\partial^2 \Lambda}{\partial p_k \partial p_l} \\
&+ \frac{\partial^2 D_{RR}}{\partial p_k \partial p_l}\Psi^- + \frac{\partial D_{RR}}{\partial p_k}\frac{\partial \Psi-}{\partial p_l} + \frac{\partial D_{RR}}{\partial p_l}\frac{\partial \Psi-}{\partial p_k} + D_{RR}\frac{\partial^2 \Psi^-}{\partial p_k \partial p_l}
\end{aligned} \tag{C.7}$$

References

[1] D. J. Mead, Free wave propagation in periodically supported, infinite beams, Journal of Sound and Vibration 11 (1970) 181–197. doi:10.1016/S0022-460X(70)80062-1.

[2] D. J. Mead, A general theory of harmonic wave propagation in linear periodic systems with multiple coupling, Journal of Sound and Vibration 27 (1973) 235–260. doi:10.1016/0022-460X(73)90064-3.

[3] D. J. Mead, The forced vibration of one-dimensional multi-coupled periodic structures: An application to finite element analysis, Journal of Sound and Vibration 319 (2009) 282–304. doi:10.1016/j.jsv.2008.05.026.

[4] M. Collet, M. Ouisse, M. Ruzzene, M. N. Ichchou, Floquet-Bloch decomposition for the computation of dispersion of two-dimensional periodic, damped mechanical systems, International Journal of Solids and Structures 48 (2011) 2837–2848. URL: `http://dx.doi.org/10.1016/j.ijsolstr.2011.06.002`. doi:10.1016/j.ijsolstr.2011.06.002.

[5] A. Nateghi, L. Van Belle, C. Claeys, E. Deckers, B. Pluymers, W. Desmet, Wave propagation in locally resonant cylindrically curved metamaterial panels, International Journal of Mechanical Sciences 127 (2017) 73–90. URL: http://dx.doi.org/10.1016/j.ijmecsci.2016.07.003. doi:10.1016/j.ijmecsci.2016.07.003.

[6] X. Xiao, Z. He, E. Li, A. Cheng, Design multi-stopband laminate acoustic metamaterials for structural-acoustic coupled system, Mechanical Systems and Signal Processing 115 (2019) 418 – 433. URL: http://www.sciencedirect.com/science/article/pii/S0888327018303406. doi:https://doi.org/10.1016/j.ymssp.2018.06.004.

[7] Z. He, X. Xiao, E. Li, Design for structural vibration suppression in laminate acoustic metamaterials, Composites Part B: Engineering 131 (2017) 237 – 252. URL: http://www.sciencedirect.com/science/article/pii/S1359836817307187. doi:https://doi.org/10.1016/j.compositesb.2017.07.076.

[8] A. O. Krushynska, M. Miniaci, F. Bosia, N. M. Pugno, Coupling local resonance with Bragg band gaps in single-phase mechanical metamaterials, Extreme Mechanics Letters 12 (2017) 30–36. URL: http://dx.doi.org/10.1016/j.eml.2016.10.004. doi:10.1016/j.eml.2016.10.004.

[9] C. Claeys, N. G. Rocha de Melo Filho, L. Van Belle, E. Deckers, W. Desmet, Design and validation of metamaterials for multiple structural stop bands in waveguides, Extreme Mechanics Letters 12 (2017) 7–22. URL: http://dx.doi.org/10.1016/j.eml.2016.08.005. doi:10.1016/j.eml.2016.08.005.

[10] S. Hedayatrasa, K. Abhary, M. Uddin, C. T. Ng, Optimum design of phononic crystal perforated plate structures for widest bandgap of fundamental guided wave modes and maximized in-plane stiffness, Journal of the Mechanics and Physics of Solids 89 (2016) 31–58. URL: http://dx.doi.org/10.1016/j.jmps.2016.01.010. doi:10.1016/j.jmps.2016.01.010.

[11] S. Hedayatrasa, M. Kersemans, K. Abhary, M. Uddin, J. K. Guest, W. Van Paepegem, Maximizing bandgap width and in-plane stiffness of porous phononic plates for tailoring flexural guided waves: Topology optimization and experimental validation, Mechanics of Materials 105 (2017) 188–203. URL: http://dx.doi.org/10.1016/j.mechmat.2016.12.003. doi:10.1016/j.mechmat.2016.12.003.

[12] E. Andreassen, H. R. Chang, M. Ruzzene, J. S. Jensen, Optimization of directional elastic energy propagation, Journal of Sound and Vibration 379 (2016) 53–70. URL: http://dx.doi.org/10.1016/j.jsv.2016.03.002. doi:10.1016/j.jsv.2016.03.002.

[13] M. Xiao, Z. Q. Zhang, C. T. Chan, Surface impedance and bulk band geometric phases in one-dimensional systems, Physical Review X 4 (2014) 1–12. doi:10.1103/PhysRevX.4.021017.

[14] R. Süsstrunk, S. D. Huber, Observation of phononic helical edge states in a mechanical topological insulator., Science (New York, N.Y.) 349 (2015) 47–50. URL: http://www.ncbi.nlm.nih.gov/pubmed/26138969. doi:10.1126/science.aab0239.

[15] R. K. Pal, M. Schaeffer, M. Ruzzene, Helical edge states and topological phase transitions in phononic systems using bi-layered lattices, Journal of Applied Physics 119 (2016). doi:10.1063/1.4942357.

[16] J. Zak, Berrys phase for energy bands in solids, Physical Review Letters 62 (1989) 2747–2750. doi:10.1103/PhysRevLett.62.2747.

[17] L. Sangiuliano, E. Deckers, C. Claeys, Control of edge modes in finite vibro-acoustic resonant metamaterials, in: Proceedings of ISMA2018-USD2018, 2018.

[18] K.-H. Chew, K. Tai, E. Ng, M. Muskulus, Analytical gradient-based optimization of offshore wind turbine substructures under fatigue and extreme loads, Marine Structures 47 (2016) 23 – 41. URL: http://www.sciencedirect.com/science/article/pii/S095183391630017X. doi:https://doi.org/10.1016/j.marstruc.2016.03.002.

[19] A. van de Walle, L. Rouleau, E. Deckers, W. Desmet, Parametric model-order reduction for viscoelastic finite element models: an application to material parameter identification, in: Proceedings of the 22nd International Congress on Sound and Vibration, INT INST ACOUSTICS & VIBRATION, 2015.

[20] L. Rouleau, B. Pluymers, W. Desmet, Characterisation of viscoelastic layers in sandwich lightweight panels through inverse techniques, in: INTER-NOISE and NOISE-CON Congress and Conference Proceedings, volume 251, Institute of Noise Control Engineering, 2015, pp. 759–769.

[21] A. Wagner, G. Spelsberg-Korspeter, P. Hagedorn, Structural optimization of an asymmetric automotive brake disc with cooling channels to avoid squeal, Journal of Sound and Vibration 333 (2014) 1888 – 1898. URL:

http://www.sciencedirect.com/science/article/pii/S0022460X13009887. doi:https://doi.org/10.1016/j.jsv.2013.11.035.

[22] J. Nocedal, S. Wright, Numerical optimization, series in operations research and financial engineering, 2006. URL: http://www.lavoisier.fr/livre/notice.asp?id=O2SWL2AO2O2OWB.

[23] Y. Dauphin, R. Pascanu, C. Gulcehre, K. Cho, S. Ganguli, Y. Bengio, Identifying and attacking the saddle point problem in high-dimensional non-convex optimization (2014) 1–9. URL: http://arxiv.org/abs/1406.2572. arXiv:1406.2572.

[24] R. Pascanu, Y. N. Dauphin, S. Ganguli, Y. Bengio, On the saddle point problem for non-convex optimization (2014). URL: https://arxiv.org/abs/1405.4604. arXiv:1405.4604.

[25] J. M. Mencik, M. N. Ichchou, Multi-mode propagation and diffusion in structures through finite elements, European Journal of Mechanics, A/Solids 24 (2005) 877–898. doi:10.1016/j.euromechsol.2005.05.004.

[26] Y. Waki, B. R. Mace, M. J. Brennan, Numerical issues concerning the wave and finite element method for free and forced vibrations of waveguides, Journal of Sound and Vibration 327 (2009) 92–108. URL: http://dx.doi.org/10.1016/j.jsv.2009.06.005. doi:10.1016/j.jsv.2009.06.005.

[27] M. N. Ichchou, S. Akrout, J. M. Mencik, Guided waves group and energy velocities via finite elements, Journal of Sound and Vibration 305 (2007) 931–944. doi:10.1016/j.jsv.2007.05.007.

[28] D. Duhamel, B. R. Mace, M. J. Brennan, Finite element analysis of the vibrations of waveguides and periodic structures, Journal of Sound and Vibration 294 (2006) 205–220. doi:10.1016/j.jsv.2005.11.014. arXiv:1010.1724.

[29] Y. Cai, J. Qian, On Some Inverse Eigenvalue Problems of Quadratic Palindromic Systems (2016) 1–22. URL: http://arxiv.org/abs/1606.03840. arXiv:1606.03840.

[30] C. W. Zhou, J. P. Lainé, M. N. Ichchou, A. M. Zine, Multi-scale modelling for two-dimensional periodic structures using a combined mode/wave based approach, Computers and Structures 154 (2015) 145–162. URL: http://dx.doi.org/10.1016/j.compstruc.2015.03.006. doi:10.1016/j.compstruc.2015.03.006.

[31] C. Droz, C. Zhou, M. N. Ichchou, J. P. Lainé, A hybrid wave-mode formulation for the vibro-acoustic analysis of 2D periodic structures, Journal of Sound and Vibration 363 (2016) 285–302. URL: http://dx.doi.org/10.1016/j.jsv.2015.11.003. doi:10.1016/j.jsv.2015.11.003.

[32] F. Maurin, C. Claeys, E. Deckers, W. Desmet, Probability that a band-gap extremum is located on the irreducible Brillouin-zone contour for the 17 different plane crystallographic lattices, International Journal of Solids and Structures 135 (2018) 26–36. URL: https://doi.org/10.1016/j.ijsolstr.2017.11.006. doi:10.1016/j.ijsolstr.2017.11.006.

[33] T. Lefebvre, F. De Belie, G. Crevecoeur, A Radial Basis Function based Optimization Algorithm with Regular Simplex set geometry in Ellipsoidal Trust-Regions (2018). URL: http://arxiv.org/abs/1805.11830. arXiv:1805.11830.

[34] J.-L. Christen, M. Ichchou, A. Zine, B. Troclet, Wave Finite Element Formulation of the Acoustic Transmission Through Complex Infinite Plates, Acta Acustica united with Acustica 102 (2016) 984–991. doi:10.3813/aaa.919013.